4

Lunar tectonics

Thomas R. Watters

Center for Earth and Planetary Studies, National Air and Space Museum, Smithsonian Institution, Washington, DC

and

Catherine L. Johnson

Earth and Ocean Sciences, University of British Columbia, Vancouver, Canada

Summary

Tectonic landforms on the Moon predominantly occur on the nearside, associated directly with the lunar maria. Basin-localized lunar tectonics is expressed by two landforms: wrinkle ridges, and linear and arcuate rilles or troughs. Wrinkle ridges are complex morphologic landforms found in mare basalts, interpreted to be contractional tectonic landforms formed by thrust faulting and folding. Linear and arcuate rilles are long, narrow troughs, interpreted to be graben formed by extension, deforming both mare basalts at basin margins and the highlands adjacent to the basins. In contrast to basin-localized tectonics, landforms of the nearside are the more broadly distributed lobate scarps. Lobate scarps on the Moon are relatively small-scale asymmetric landforms that are often segmented with lobate margins. These landforms are the surface expression of thrust faults and are the dominant tectonic feature on the lunar farside. Crater density ages indicate that crustal extension associated with lunar maria ceased at ~3.6 Ga. Crustal shortening in the maria, however, continued to as recently as ~1.2 Ga. The cessation of extension may have resulted from the superposition of compressional stresses from global contraction on flexural extensional stress due to loading from the mare basalts. The lobate scarps formed less than 1 Ga and appear to be among the youngest endogenic features on the Moon. The presence of young lobate scarp thrust faults supports late-stage compression of the lunar crust. Lunar seismic data provide insight into the lunar interior structure, and the spatial distribution and depth of some moonquakes suggests current tectonic activity on the Moon. Deep moonquakes tend to cluster around edges of, or beneath, the nearside

Planetary Tectonics, edited by Thomas R. Watters and Richard A. Schultz. Published by Cambridge University Press.

basins. Although too deep to be directly correlated with the distribution of tectonic features, they may be related to long-lived, deep lateral thermal and/or compositional heterogeneities associated with either basin formation and/or mare basalt production. Shallow-depth moonquakes are also distributed around the nearside basins. Depths of these quakes are poorly constrained; although some arguments favor an upper mantle origin, it is plausible that at least some quakes occur within the lunar crust. Thus, some moonquakes may be associated with the observed lunar faults. Current lunar gravity models show that anomalies for the mare mascons have broad plateaus throughout the mare interior. The shoulders of the positive anomalies spatially correlate with basin-interior rings of wrinkle ridges and suggest a pan- rather than a bowl-shaped mare-fill geometry. Recent mascon stress models suggest that a more uniform thickness of mare basalts best fits the observed spatial distribution of the wrinkle ridges and linear and arcuate rilles. The contractional strain expressed by the relatively young lobate scarps is estimated to be ~0.008% over an area of roughly 10% of the lunar surface. If representative of the entire surface, this strain corresponds to a radius change of ~70 m, consistent with thermal history models that predict a small change in lunar radius in the last 3.8 Ga.

1 Introduction

The Moon has many characteristics that distinguish it from other moons and satellites in the solar system. This is particularly true in the context of planetary tectonics. Its greatest distinction is, of course, the fact that it is the only other body in the solar system that humans have explored from the surface. The Apollo 17 astronauts were the last to visit the Moon and the first to make a field examination of a fault scarp on another planetary body. The Lee-Lincoln scarp is not a very imposing structure in the landscape of the Apollo 17 landing site (Figure 4.1); the latter is dominated by the several kilometer-high mountains of the North and South Massif. However, when astronauts Eugene A. Cernan and Harrison H. Schmitt attempted to drive straight up the scarp face with the Lunar Roving Vehicle (LRV), the wheels began to slip, and they had to steer across-slope to reach the top, some 80 m above the lower floor of the Taurus-Littrow valley. The Lee-Lincoln scarp exemplifies an important class of lunar faults, lobate scarp thrust faults.

The dark maria are prominent features of the nearside, visible from Earth even with the naked eye because of their albedo contrast with the bright terrae or highlands. It is now well known that the maria are basalts that flooded topographic lows created by large impact events. The vast majority of the Moon's large-scale tectonic features are found in the basalt-filled impact basins and the adjacent highlands. The dominant tectonic landforms that resulted from this basin-localized

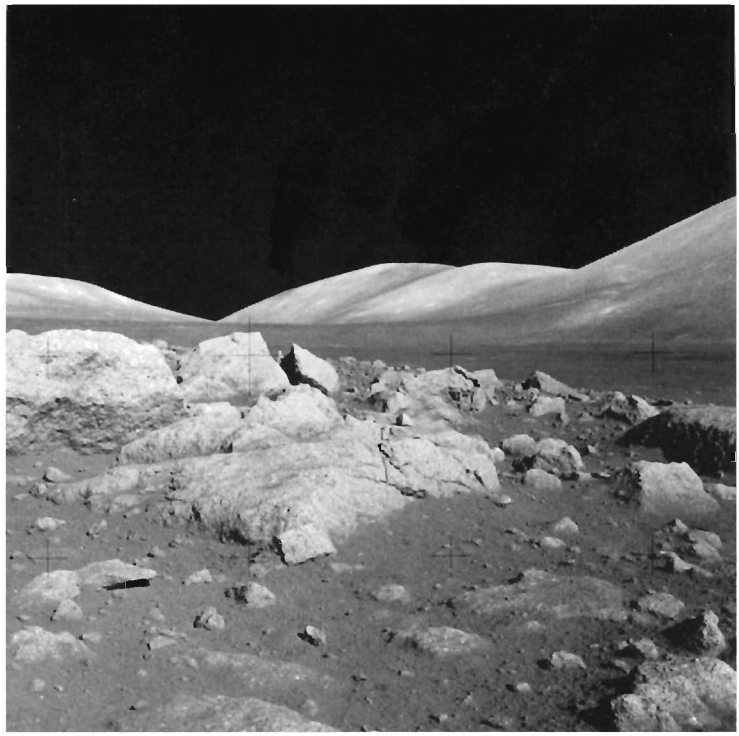

Figure 4.1. Tauras-Littrow valley near the Apollo 17 landing site. The Lee-Lincoln scarp is in the foreground, with the hills of Family Mountain in the background. The fault scarp offsets the floor of the Tauras-Littrow valley (Hasselblad Camera frame AS17-134-20443).

deformation on the Moon are wrinkle ridges, and linear and arcuate troughs or rilles (Plates 6A,B).

Wrinkle ridges are morphologically complex landforms that occur in mare basalts. In fact, they are often referred to as mare ridges because of their direct association with the maria (see Plates 6A,B) (see Head, 1976; Wilhelms, 1987). Their morphologic complexity is generally attributable to the superimposition of two landforms, a broad arch and a narrow ridge. Wrinkle ridges were first discovered and mapped using Earth-based telescopic observations of the lunar maria (Figure 4.2) (Gilbert, 1893; Fielder, 1961; Baldwin, 1963, 1965). Although interpreted to be anticlinal forms over a hundred years ago by Gilbert (1893), other investigators concluded that wrinkle ridges were volcanic features related to the emplacement of the mare basalts or the result of intrusion or extrusion of lava into fractures and zones of weakness following crustal extension related to basin-localized or global tectonic patterns (Fielder, 1961; Quaide, 1965; Whitaker, 1966; Tjia, 1970; Hartman and Wood, 1971; Colten *et al.*, 1972; Strom, 1972; Hodges, 1973; Scott,

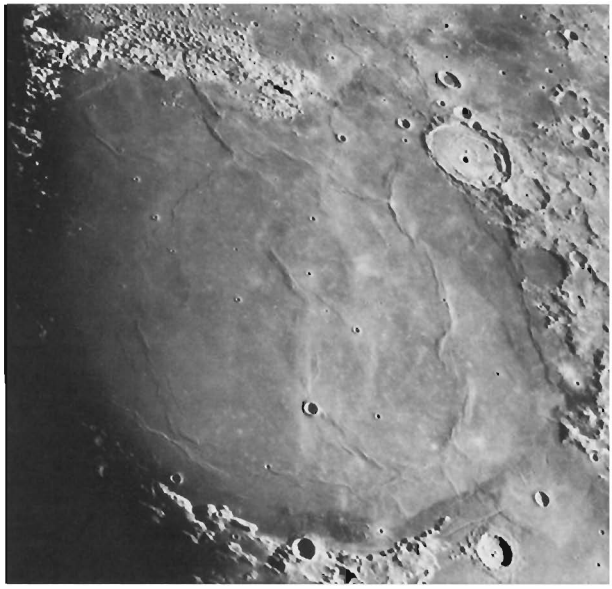

Figure 4.2. Earth-based telescope view of Mare Serenitatis. Wrinkle ridges formed in the mare basalts are prominent landforms in low sun angle telescope observations. Rilles, long, narrow arcuate or linear troughs are also discernable (near the southwestern margin of Serenitatis). The image (Photo Number C1487) is from the Consolidated Lunar Atlas (Lunar and Planetary Laboratory, University of Arizona, 1967).

1973; Young *et al.*, 1973). Others concluded, as Gilbert had, that mare ridges are purely tectonic landforms (Baldwin, 1963, 1965; Bryan, 1973; Hodges, 1973; Howard and Muehlberger, 1973; Schaber, 1973a; Muehlberger, 1974; Maxwell *et al.*, 1975; Lucchitta, 1976, 1977; Maxwell, 1978; Sharpton and Head, 1981, 1982, 1988). Circular wrinkle ridges or wrinkle-ridge rings and basin-concentric ridge patterns (Plate 6A) were cited as evidence that subsidence of the mare basalts played an important role in their formation (Wilhelms and McCauley, 1971; Maxwell *et al.*, 1975; Brennan, 1976). Perhaps the most convincing support for a structural interpretation of mare ridges is the subsurface information provided by the Apollo Lunar Sounder Experiment (ALSE) data (Phillips *et al.*, 1973; Peeples *et al.*, 1978; Maxwell and Phillips, 1978). ALSE data over a mare ridge in southeastern Mare Serenitatis show evidence of an anticlinal rise in subsurface horizons and thinning of a mare unit (sequence of flows) on apparent structural relief (Maxwell, 1978). A compressional tectonic origin involving a combination of folding and thrust faulting is also supported by studies of terrestrial analogues (Plescia and Golombek, 1986; Watters, 1988). The tectonic interpretation of wrinkle ridges subsequently found on Mercury, Venus, and Mars is rooted in the early analysis of mare ridges. In the study of planetary wrinkle ridges, the volcanic versus tectonic debate has been replaced by general disagreement over the relative role of folding and faulting, the geometry and number of thrust faults, and whether faults are surface breaking or non-surface breaking (blind) (e.g., Golombek *et al.*, 1991; Watters, 1992; Schultz, 2000; Golombek *et al.*, 2001; Mueller and Golombek, 2004; Watters, 2004).

Rilles were also identified in Earth-based telescopic surveys of the Moon (Figure 4.2). They are long, narrow troughs that commonly exhibit three plan-view

geometries: sinuous, arcuate, and linear. Because sinuous rilles are meandrous and confined to mare basalts they are interpreted to be volcanic in origin. Sinuous rilles are generally thought to be collapsed lava tubes or lava channels (Greeley, 1971; Schultz, 1976a; Masursky *et al.*, 1978; Wilhelms, 1987; Spudis *et al.*, 1988a). The relationship between sinuous rilles and mare ridges has been cited as evidence that some elements of wrinkle ridges are volcanic in origin (Greeley and Spudis, 1978). Linear and arcuate rilles are found in the highlands adjacent to, and in the margins of mare basins and generally have basin-concentric orientations (Plates 6A,B) (see McGill, 1971; Golombek, 1979; Wilhelms, 1987). In cross section, these rilles are flat-floored with steep walls. This cross-sectional geometry and the fact that the trough walls maintain roughly the same relief as they extend from mare basalts into basin rim or highlands material has led to the interpretation that rilles are formed by graben (Baldwin, 1963; Quaide, 1965; McGill, 1971; Golombek, 1979). Like terrestrial and other planetary graben, many lunar rilles are segmented with echelon steps indicating that the faults grow by segment linkage (see McGill, 2000). Less common than basin-concentric graben are basin-radial graben (Plate 6A). These graben are dominated by linear rille segments, many of which are radial or subradial to the Imbrium basin (Quaide, 1965; Wilhelms, 1987). Relatively small depressions that occur near or at intersections of linear rilles have been interpreted as possible sites of recent out-gassing from sources deep in the lunar interior (Schultz *et al.*, 2006).

It is clear that the mare ridges and the arcuate and linear rilles are indicative of a pattern of basin-localized contractional and extensional deformation (Plates 6A,B). Thus the types, locations, and relative timing of these two classes of tectonic features have been used to provide constraints on the tectonic evolution of the mare-filled nearside lunar basins (e.g., Phillips *et al.*, 1972; Melosh, 1978; Solomon and Head, 1979, 1980; Freed *et al.*, 2001). The combination of a mass concentration from the mare basalts (mascon) and an impact-induced thinned and weakened lithosphere is responsible for what is referred to as mascon tectonics, resulting in the observed spatial patterns of deformation.

Although lunar tectonics, in contrast to terrestrial planets like Mercury, Venus, and Mars, is largely basin-localized, lobate scarps is a class of tectonic landform on the Moon that is not directly associated with the mare basins. Analogous to tectonic landforms found on Mercury (Watters *et al.*, 1998, 2001, 2004; Watters and Nimmo, Chapter 2) and Mars (Watters, 1993, 2003; Watters and Robinson, 1999; Golombek and Phillips, Chapter 5), lunar lobate scarps are generally asymmetric landforms and are often lobate and segmented. The most significant contrast between planetary and lunar lobate scarps is scale. While lobate scarps on Mercury and Mars can have over a kilometer of relief, lunar scarps have a maximum relief of only tens of meters (Howard and Muehlberger, 1973; Lucchitta, 1976; Binder, 1982; Binder and Gunga, 1985). The lengths of the lunar scarps are proportionately smaller,

reaching a maximum of only tens of kilometers (Binder and Gunga, 1985). Lunar lobate scarps, like their planetary counterparts, are interpreted to be the result of thrust faulting (Howard and Muehlberger, 1973; Lucchitta, 1976; Binder, 1982; Binder and Gunga, 1985). The evidence of offset is not as dramatic as in the case of large-scale lobate scarps on Mercury and Mars, however, the morphology and the linkage between individual segments of the lunar scarps supports the interpretation that they are the surface expression of shallow thrust faults. Although many of the lunar lobate scarps are found in the highlands (Plates 6A,B), there are some cases where scarps are associated with wrinkle ridges. The structures have been described as "mare–ridge, highland–scarp systems" (Lucchitta, 1976). The source of compressional stresses that formed the lobate scarps has been suggested to be thermal stresses from global cooling (Solomon and Chaiken, 1976; Solomon and Head, 1979; Binder and Lange, 1980). If so, the spatial distribution and scale of the lunar scarps has important implications for the Moon's thermal history and for constraining models for its origin.

The Moon is also unique in our solar system, because it is the only other body for which we have *in situ* seismic data. Data recorded by seismometers at Apollo sites 12, 14, 15 and 16, over the period 1969–1977, show that the Moon is seismically active, exhibiting present-day quakes in two depth ranges: shallow moonquakes occurring at depths of 100 km or less, and deep moonquakes occurring at depths of 700–1000 km. The deep moonquakes are numerous (many thousands recorded), and very early on during the Apollo era were observed to exhibit tidal periods. Repeatable or coherent seismograms have been interpreted as events that originate from the same location – thus, although many thousands of deep moonquakes have been identified, they appear to originate from only 100–200 source regions. Shallow moonquakes have been interpreted to be tectonic in origin, and so their locations with respect to tectonic features on the Moon are of interest. In addition to the location and timing of events, the seismic data provides information on the interior structure of the Moon to depths of about 1000 km.

The scale and complexity of lunar tectonics does not rival that on the terrestrial planets or even that on some of the icy moons of the outer planets. It is nonetheless important because the pre- and early-robotic and human investigation of lunar tectonic landforms is the foundation and touchstone for subsequent interpretation and analysis of crustal deformation on other bodies in the solar system. Our understanding of lunar tectonics is far from complete. To date, less than roughly 10% of the lunar surface has been imaged at high enough resolution and optimal illumination conditions to detect small-scale tectonic features such as the highland lobate scarps. With the international armada of new lunar robotic missions and the U.S. initiative to return humans to the Moon, the opportunity to fully explore lunar tectonics is close at hand.

In this chapter, we will describe the known tectonic landforms on the Moon, their spatial distribution, and the timing of their formation. The relationship between the tectonic features, the lunar maria, and the topography and the gravity field of mare basins is examined. Lunar seismicity and our current understanding of the Moon's interior structure are reviewed and the correlation between moonquakes and nearside tectonism is evaluated. Mascon stress models are considered in light of current topography and gravity data. The strain and contraction from lobate scarp thrust faults is estimated and implications for the thermal history models discussed. Finally, outstanding questions about the tectonic evolution of the Moon are identified and explored in the context of new data from upcoming missions.

2 Tectonic features of Moon

A full morphological description and characterization of lunar tectonic landforms requires high-resolution imaging as well as topographic data. Current topographic data sets for the Moon afford different resolution and accuracy, depending on the geographical region under study. We briefly review available topographic data sets, before turning to more detailed discussions of the tectonic features.

Early attempts to measure the topography of lunar features were made using telescope-based shadow measurements (Wu and Doyle, 1990). The Ranger spacecrafts and the Lunar Orbiters provided the first space-based stereo images used to derive lunar topographic maps. The highest quality Apollo-era topography was derived from the Apollo 15, 16, and 17 Metric (25–30 m resolution) and Panoramic (1–2 m resolution) cameras' stereo photography. These photographs were used to generate the Lunar Topographic Orthophotomap (LTO) series at scales of 1:250 000 down to 1:10 000 by means of analogue stereoplotters (Wu and Doyle, 1990). However, the Apollo spacecraft were confined to lunar equatorial orbits, limiting the coverage of the LTOs. Limited topographic profiles were obtained by Apollos 15, 16, and 17 from laser altimeters attached to the metric camera systems (e.g., Wollenhaupt *et al.*, 1973), and by the Apollo 17 Lunar Sounder Experiment (Phillips *et al.*, 1973; Peeples *et al.*, 1978; Maxwell and Phillips, 1978; Sharpton, 1992).

Nearly global topography of the Moon was obtained by the laser ranging instrument (LIDAR) flown on the Clementine spacecraft. The LIDAR instrument collected topographic data between 75°S and 75°N latitude (see Nozette *et al.*, 1994). Clementine's polar orbit provided altimetry data along north–south orbital tracks (roughly along lines of longitude) spaced by approximately 2.5° at the equator (~75 km) (Spudis *et al.*, 1994; Zuber *et al.*, 1994). The distribution of good returns is highly variable within an orbital track because of the influence of terrain roughness and solar phase angle (Spudis *et al.*, 1994). The single-shot ranging precision

of the LIDAR (vertical resolution) is estimated to be 40 m (Zuber *et al.*, 1994). Some of the highest along-track resolution was obtained over smooth mare surfaces, late in the mission when solar phase angles where larger (Smith *et al.*, 1997).

Earth-based radar interferometry has been used to determine the topography of the polar regions where no Clementine LIDAR data was collected (Margot *et al.*, 1998, 1999). Using digital stereo methods, Clementine ultraviolet-visible (UVVIS) nadir and off-nadir stereo images were used to produce Digital Elevation Models (DEMs) for the polar regions beyond that covered by Earth-based radar and globally (Cook *et al.*, 2000; U.S. Geological Survey, 2002; Rosiek *et al.*, 2007). The nadir-pointing Clementine UVVIS images are not ideal because the stereo angle between adjacent UVVIS images is generally weak (3° to 5°) and the lighting geometry was not optimized for morphologic studies. Stereo images from the Galileo spacecraft flyby in 1992 have also been used to generate a DEM of the lunar north polar region (Schenk and Bussey, 2004). At present, the highest resolution stereo images of the lunar surface are from the Apollo Metric and Panoramic cameras.

2.1 Wrinkle ridges

Wrinkle ridges are landforms that have been found in volcanic plains on Mercury, Venus, and Mars, and analogous structures occur in continental flood basalts on Earth (Plescia and Golombek, 1986; Watters, 1988, 1992). Mare wrinkle ridges are the most common and probably the best described of those observed on the terrestrial planets, and are found in nearly all lunar maria (Strom, 1972; Bryan, 1973; Maxwell *et al.*, 1975; Head, 1976; Plescia and Golombek, 1986; Watters, 1988; Golombek *et al.*, 1991). Mare ridges typically occur both radial to and concentric with the centers of mare basins (Bryan, 1973; Maxwell *et al.*, 1975) (Plates 6A,B, Figure 4.3). The association between wrinkle ridges, maria and mare basalts has led some workers to suggest a genetic relation between the basalts and the origin of the structures (see Strom, 1972; Bryan, 1973; Watters, 1988).

Mare wrinkle ridges and their planetary counterparts are morphologically complex structures that may be composed of a number of superimposed landforms, often consisting of a composite of a broad arch and narrow, asymmetric ridges (Figures 4.3, 4.4). These morphologic elements may also occur independently of one another. Arches are broad, gently sloping, curvilinear topographic rises that are commonly asymmetric in profile and often only distinguishable in low sun angle images (Figure 4.4) (Strom, 1972; Bryan, 1973; Maxwell *et al.*, 1975). Ridges are long, relatively narrow, segmented features that are commonly strongly asymmetric in cross section. The sense of the asymmetry may change either along strike or from one ridge segment to the next, and segments often occur in en-echelon

Figure 4.3. Apollo Metric Camera mosaic of part of southern Mare Serenitatis. Wrinkle ridges, also described as mare ridges, are morphologically complex features often composed of a number of superimposed landforms. Both basin-concentric and basin-radial wrinkle ridges occur in Mare Serenitatis. Arcuate rilles or troughs occur near the basin margin. The mosaic was generated using Metric camera frames AS17-450 and AS17-454.

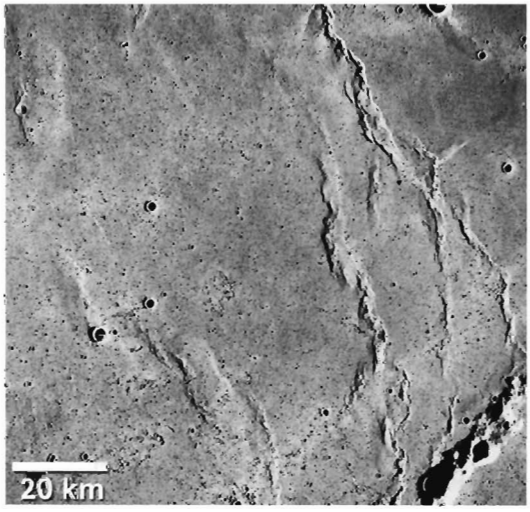

Figure 4.4. Mare ridge in Oceanus Procellarum near the northwestern edge of the Aristarchus Plateau (lower left). Wrinkle ridges often consist of broad, low-relief arches and superposed, narrow ridges (Apollo 15 Metric Camera AS15-2487).

arrangements (see Tjia, 1970). In wrinkle-ridge assemblages in mare basins, the ridge is often superposed on the arch (Strom, 1972; Bryan, 1973; Maxwell *et al.*, 1975).

In addition to this ridge–arch association, there is evidence of smaller secondary ridges that occur on or near larger primary ridges. These second-order mare ridges

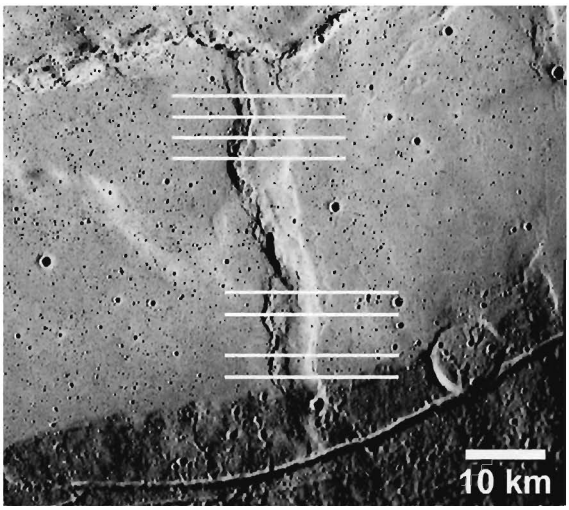

Figure 4.5. The morphology of wrinkle ridge Dorsum Nicol in Mare Serenitatis. The complex morphology of this prominent wrinkle ridge is the result of several superposed landforms (Metric Camera frames AS-17-453).

are sharp, narrow prominences that are very similar in morphology to the first-order ridges and commonly flank or cap the larger ridges (Watters, 1988). Even smaller third-order ridges can be found that flank or commonly cap larger ridges. These small-scale ridges can only be easily resolved in Apollo Metric Camera and Panoramic Camera images (see Scott, 1973; Watters, 1988).

2.1.1 Topography of wrinkle ridges

The best available topography for lunar wrinkle ridges is from Lunar Topographic Orthophotomaps. The morphology and dimensions of a number of wrinkle ridges in Mare Serenitatis, Mare Imbrium, and Mare Procellarum have been described using these data (Watters, 1988; Golombek *et al.*, 1991). High-resolution Apollo Metric and Panoramic Camera images and stereo derived topography illustrate the distinct morphology elements of these landforms (Figure 4.5); the broad rise or arch and the superposed ridge. Using the LTOs, the maximum relief of 12 wrinkle-ridge segments was measured (Table 4.1). The maximum relief of the measured ridges varies from about 50 to 410 m (mean ~253 m), in agreement with previous surveys (Watters, 1988; Golombek *et al.*, 1991). Topographic profiles across Dorsum Nicol in Mare Serenitatis show that the vergent side of the ridge changes along strike (Figure 4.6). The vergence may change either along strike or from one ridge segment to the next. Changes in vergence is a common characteristic of wrinkle ridges on the Moon, Mercury, and Mars and terrestrial analogues such as the anticlinal ridges of the Columbia Plateau in the northwestern United States (see Reidel, 1984; Watters, 1988, 1991, 1992, 2004).

Clementine LIDAR profiles provide excellent long-wavelength topography of mare surfaces (Smith *et al.*, 1997). In rare cases, the along-track spatial resolution

Table 4.1 *Dimensions of wrinkle ridges on the Moon*

Index	Latitude	Longitude	Maximum Relief (m)	Length (km)	D $\theta = 30°$ (m)
Dorsum Nicol	18.5°N	22.8°E	240	49	480
Dorsum Lister S	20°N	23.3°E	408	79	816
Dorsum Lister N	21.2°N	24.8°E	358	61	716
Dorsum Lister W	19.5°N	19.5°E	262	49	524
Dorsum Zirkel	30°N	25.5°W	272	145	544
Dorsum Buckland E	18.3°N	19.5°W	207	80	414
Dorsum Buckland Mid	18.8°N	17.5°W	223	24	446
Dorsum Buckland W	19.3°N	16°E	238	35	476
Dorsa Ewing	29.2°N	24.5°W	309	110	618
Dorsa Rubey	9.8°S	42.3°W	48	50	96
Dorsa Smirnov	25°N	25.5°E	300	68	600
Dorsum Von Cotta	25.5°N	12°E	166	54	332

Relief was determined using Lunar Topographic Orthophotomaps (LTOs).

was high enough to resolve the cross-sectional topography of wrinkle ridges in Mare Serenitatis. LIDAR data across a segment of Dorsum Buckland (located at ~17°E) indicates the relief of the ridge is ~190 m (Figure 4.7). The maximum relief of this segment of Buckland (mid-segment, Table 4.1) determined from an LTO is ~220 m, in good agreement with the LIDAR-based measurement. The same LIDAR profile shows the long-wavelength topography of the mare surface in Serenitatis and indicates that this segment of Dorsum Buckland is imposed on a gentle regional slope (Figure 4.8). It also indicates that the center of Mare Serenitatis is higher than the margins along this transect (Watters and Konopliv, 2001). This is the case elsewhere in Mare Serenitatis. Generally, the lowest elevations of the mare surface are outside the prominent mare ridge ring in the interior (Watters and Konopliv, 2001) (Figure 4.8, Plate 7). The elevation difference between the center and the lowest elevation of the mare surface is up to 400 m, located on its southeast margin (Watters and Konopliv, 2001). A central topographic high in Mare Serenitatis is also evident in east–west profiles across the central basin, as revealed in Apollo Laser Altimeter data (see Wollenhaupt *et al.*, 1973, Fig. 33–24a) and Apollo Lunar Sounder Experiment (ALSE) data (see Sharpton, 1992, Fig. 2).

2.1.2 Elevation offsets across wrinkle ridges

It has been observed that topographic data for some mare ridges from LTOs and Apollo Lunar Sounder Experiment (ALSE) data exhibit elevation offsets from one side of a ridge to the other (Maxwell *et al.*, 1975; Lucchitta, 1976; Golombek

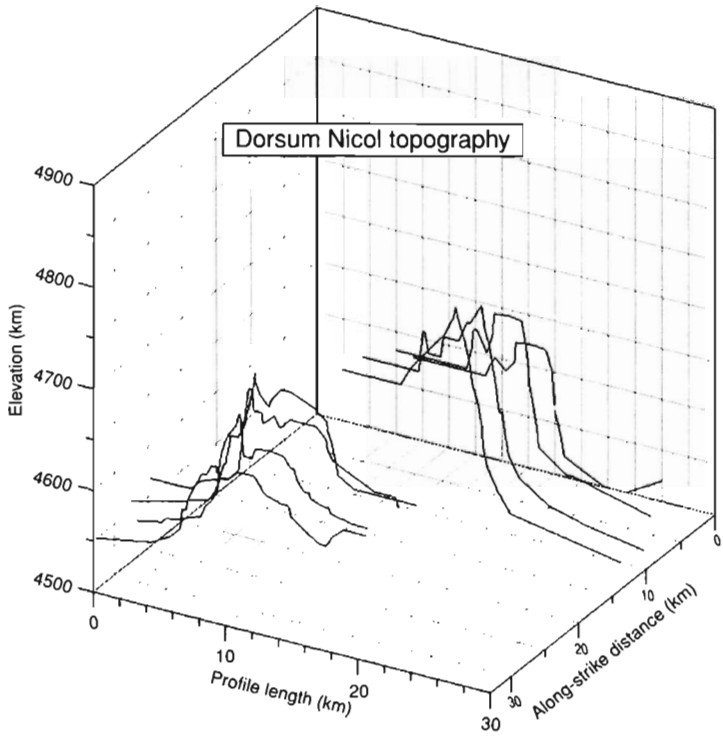

Figure 4.6. Topographic profile constructed from two 1:50 000 LTOs (42C4S1 and 42C4S2) show the major morphologic elements of wrinkle ridges. The profiles also show a reversal in the vergent side of the ridge from the northern section (upper four profiles) to the southern section (lower four profiles). The first profile (southernmost) is at the origin of the along strike distance. Profile locations are shown in Figure 4.5. Elevations are relative to an arbitrary zero vertical datum of 1 730 000 m. Vertical exaggeration is 75:1.

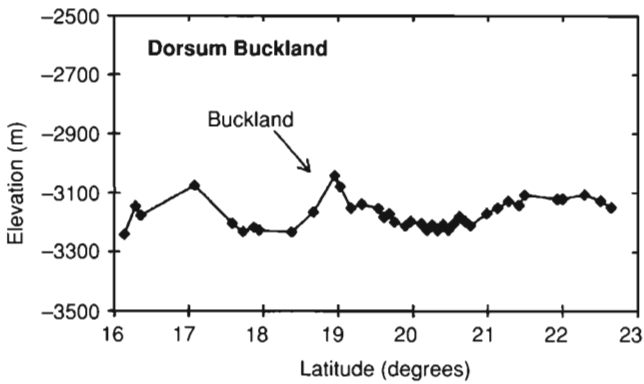

Figure 4.7. Clementine LIDAR profile located at approximately 17.25°E longitude crossing Dorsum Buckland in Mare Serenitatis. The LIDAR data were extracted from the dataset of Smith *et al.* (1997). Elevations are in meters above an ellipsoid of radius 1738 km at the equator with a flattening of 1/3234.93 corresponding to the flattening of the geoid. The vertical exaggeration is ~135:1.

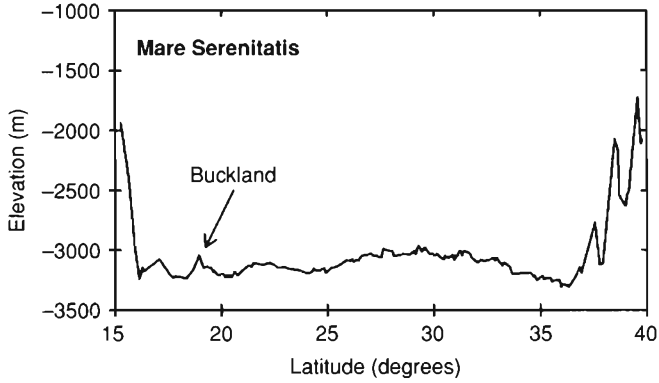

Figure 4.8. Clementine LIDAR profiles located at approximately 17.25°E longitude crossing Mare Serenitatis. The LIDAR data were extracted from the dataset of Smith *et al.* (1997). Elevations are in meters above an ellipsoid of radius 1738 km at the equator with a flattening of 1/3234.93 corresponding to the flattening of the geoid. The vertical exaggeration is ~194:1.

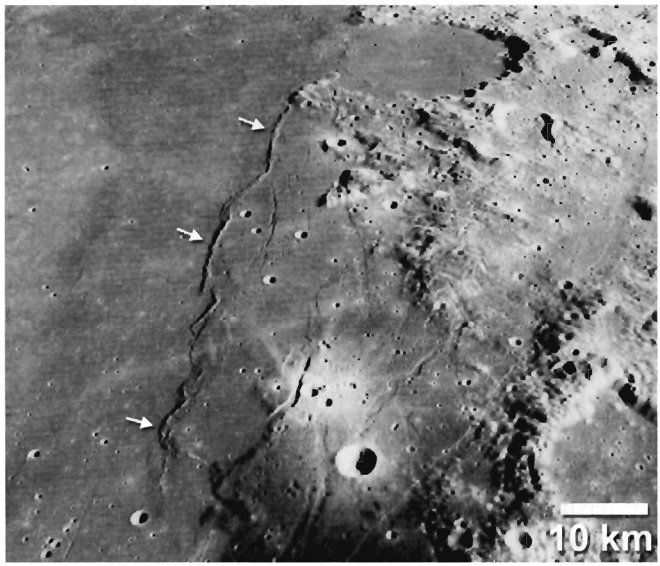

Figure 4.9. Dorsa Aldrovandi wrinkle ridge system near the eastern margin of Mare Serenitatis. Ridge segments are associated with a significant topographic offset of the mare surface with the lower elevations consistently on the interior side of the ridge. Extensional troughs (Fossae Pavlova) trend parallel to subparallel to Dorsa Aldrovandi (Metric camera frame AS17-939).

et al., 1991). The most prominent elevation offset is found on a wrinkle ridge near the eastern margin of Mare Serenitatis. Dorsa Aldrovandi is about 130 km long and segments of the ridge have offsets of as much as ~300 m, with the lower mare surface consistently on the basin-interior side of the ridge (Figure 4.9). One segment of Aldrovandi, referred to as the Littrow ridge, has linear fissures or troughs that run along the ridge crest (Figure 4.10) (Howard and Muehlberger, 1973; Maxwell *et al.*, 1975). The troughs are interpreted to be evidence of significant layer–parallel extension associated with the formation of the ridge over a high-angle reverse or

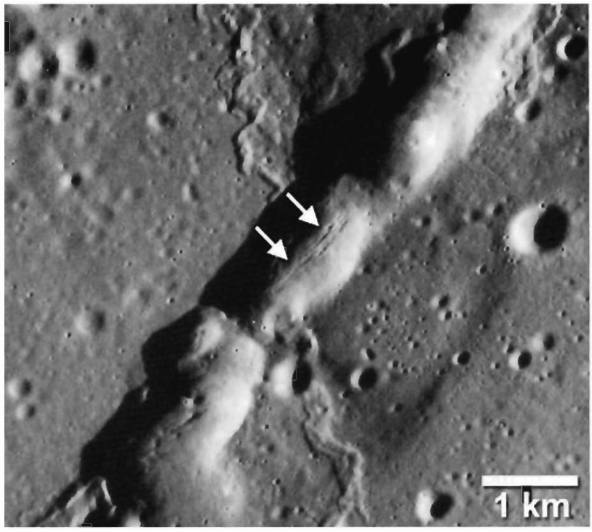

Figure 4.10. The Littrow ridge in the Taurus-Littrow region near the eastern margin of Mare Serenitatis. The lineations along the crest of the ridge (see arrows) may be evidence of layer–parallel extension resulting from folding and thrust faulting of the mare basalts (Panoramic camera frame AS17-2313).

thrust fault (Watters, 1988). A network of extensional troughs (Fossae Pavlova) also flanks Dorsa Aldrovandi on the margin side of the ridge system. These troughs trend parallel to subparallel to Aldrovandi (Figure 4.9), a rare pattern in lunar mare but common in the Caloris basin of Mercury (Watters and Nimmo, Chapter 2).

Elevation offsets across other mare ridges are not as large compared to Dorsa Aldrovandi (see Golombek *et al.*, 1991). It has been suggested that elevation offsets across mare ridges, as in the case of Dorsa Aldrovandi, are an indication of deeply rooted thrust faults (Golombek *et al.*, 1991). These deeply rooted thrust faults separate crustal material into structural blocks resulting in elevation steps of the mare surface. An alternative explanation for the elevation offsets across some of the mare ridges is that they are an artifact of regional slope, and the apparent offset is due to the short-wavelength topography of the ridge superposed on the long-wavelength topography of the mare surface (see Sharpton, 1992; Watters and Robinson, 1997). In Mare Serenitatis, for example, the lowest elevations in the basin generally lie outside the prominent ring of mare ridges in the interior (Plates 6A,B, 7). Thus, the elevation of the mare surface on the margin side appears to be lower than the interior side. The exception to this regional trend is Dorsa Aldrovandi (see above).

2.1.3 Subsurface structure at wrinkle ridges

The first application of electromagnetic (EM) sounding to planetary exploration was the Apollo 17 Lunar Sounder Experiment (ALSE). The radar sounder revealed subsurface reflecting horizons in the basalts of Mare Serenitatis and Mare Crisium (Phillips *et al.*, 1973; Peeples *et al.*, 1978; Maxwell and Phillips, 1978). Echoes from the 5 MHz frequency of ALSE indicated two subsurface reflectors at depths of 0.9

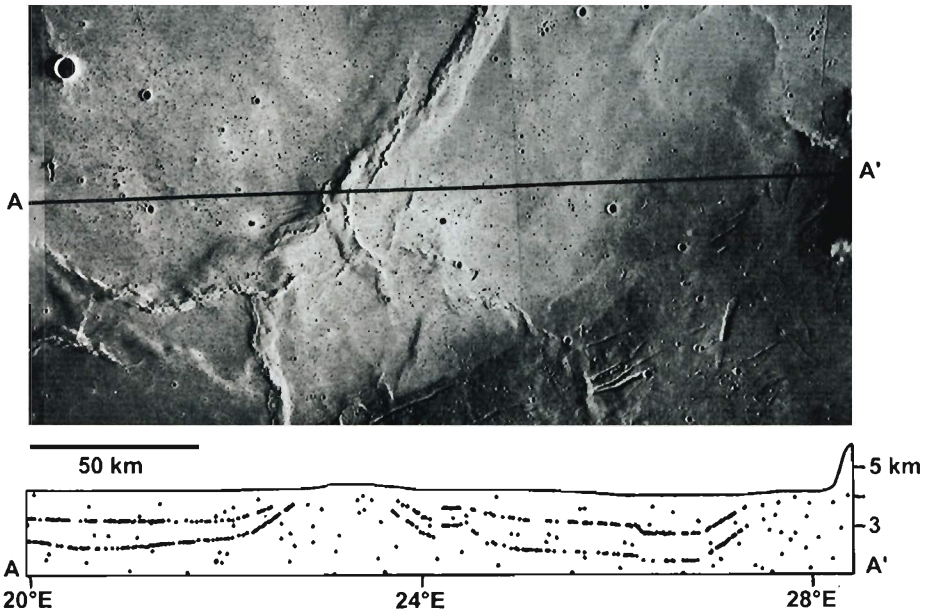

Figure 4.11. Apollo Lunar Sounder Experiment (ALSE) radar returns over part of Mare Serenitatis and a segment of the mare ridge Dorsa Lister. Echoes from the 5 MHz frequency of ALSE indicate two subsurface reflectors at depths of 0.9 and 1.6 km below the surface of Mare Serenitatis. Figure taken from Peeples *et al.*, 1978, Plate 1.

and 1.6 km below the surface of Mare Serenitatis (Figure 4.11) and at 1.4 km below the surface of Mare Crisium (Peeples *et al.*, 1978; Maxwell and Phillips, 1978). They were interpreted to be deep-lying density inversions consisting of regolith or pyroclastic deposits (Peeples *et al.*, 1978). The thicknesses of the interbeds were estimated to be on the order of several meters. Radar sounder data obtained by Kaguya also shows evidence of subsurface reflectors in Mare Serenitatis (Ono *et al.*, 2009). The ALSE data over Dorsa Lister shows that the subsurface radar reflectors dip away from the center of the ridge (Figure 4.11) (see Maxwell, 1978). The data also shows evidence of thinning of a mare unit (sequence of flows) on apparent structural relief (Maxwell, 1978). It is likely that the mare basalt thins on structural relief due to faulting and buckling over a pre-mare topographic prominence in the basin floor (see Maxwell, 1978; Sharpton and Head, 1982; Watters, 1988). Kaguya sounder data also indicate that subsurface reflectors beneath wrinkle ridges curve upward suggesting folded basalt layers (Ono *et al.*, 2009). The ring of mare ridges in Mare Serenitatis and other mare basins strongly suggests that wrinkle ridge thrust faults were localized by pre-mare topography, particularly interior basin rings (Maxwell *et al.*, 1975). These patterns of mare ridges are the only basis for identifying the location of the inner rings of Mare Serenitatis and other mare

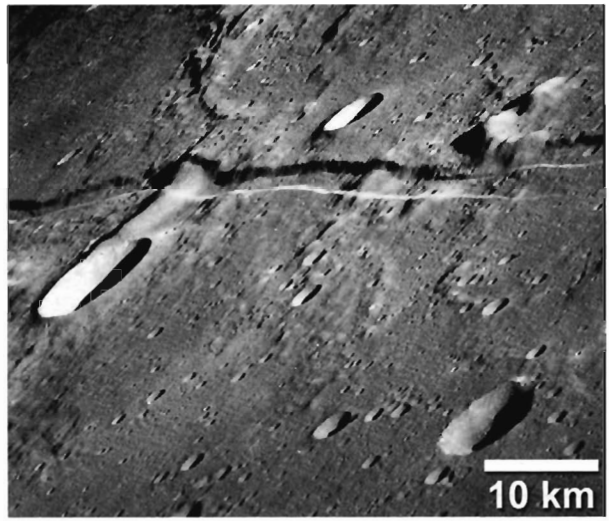

Figure 4.12. Linear graben of Rima Ariadaeus (6.5°N, 12.7°E). The troughs have a symmetric cross-sectional geometry, flat floors and steeply dipping walls. The trough walls maintain roughly the same relief in both mare basalts and highlands material suggesting that the bounding normal faults of the graben have about the same dip (Apollo Hasselblad Camera frame AS10-4645).

basins (Wilhelms, 1987). This suggests that subsurface discontinuities play a major role in localizing mare ridges. Impact craters buried by mare basalts also influence the formation of wrinkle ridges. Arcuate segments of the Dorsa Aldrovandi that include the Littrow ridge clearly indicate the influence of a buried impact crater in the basement of Mare Serenitatis (Figure 4.9). Wrinkle-ridge rings formed over shallow buried impact craters are common in ridged plains on both Mercury and Mars (Watters, 1993; Watters and Robinson, 1997; Watters and Nimmo, Chapter 2).

2.2 Lunar graben

Analogous landforms to linear and arcuate rilles or troughs, first identified in Earth-based telescopic observations, are now known to occur on Mercury, Venus, and Mars, many of the icy satellites of the outer planets, and even some small solar system objects. Their highly symmetric cross-sectional geometry and characteristic flat floors and steep inward dipping walls (Figure 4.12) have led to the nearly unanimous interpretation that they are graben formed by crustal extension (Baldwin, 1963; Quaide, 1965; McGill, 1971; Lucchitta and Watkins, 1978). The spatial correlation between linear and arcuate rilles and the nearside maria is striking (Plate 6A). Equally striking is the absence of extensional troughs on the farside (Scott *et al.*, 1977), outside of Mare Orientale (Plate 6B).

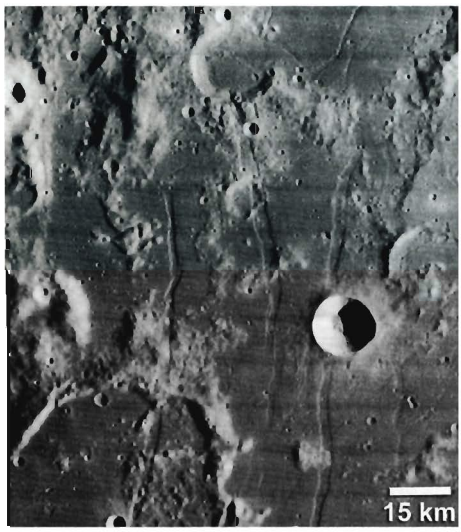

Figure 4.13. Arcuate graben system of Rimae Hippalus (23.5°S, 29°W). The graben are regularly spaced over a ~50-km wide zone east of Mare Humorum (Lunar Orbiter frame IV-132-H1).

The strongly symmetric cross-sectional geometry and the lack of offset of the trough walls across the structure (i.e., the walls maintain roughly the same relief as they extend from mare basalts into highlands material) indicate that the bounding antithetic normal faults of the graben have about the same dip (Figures 4.12, 4.13). This class of graben and analogue structures is often described as simple graben (see Golombek, 1979; Golombek and McGill, 1983). Complex graben by contrast exhibit crosscut and offset floors and walls, reflecting multiple episodes of extension. These structures are common in broad zones of crustal extension and rifting, not found on the Moon. Zones of basin-localized extension on the Moon are more distributed in nature, and graben are often regularly spaced. The most striking example is the regularly spaced, arcuate graben of Rimae Hippalus, just east of Mare Humorum (Figure 4.13).

Kinematic models for simple graben differ on the geometry of the faults as they converge at depth. One kinematic model has the two faults intersecting in a mechanical discontinuity (Golombek, 1979; Golombek and McGill, 1983). Failure initiates in the discontinuity and conjugate faults develop. In the conjugate fault model, the fault plane dip and the width of the graben expressed at the surface may be used to infer the depth of the mechanical discontinuity (Golombek, 1979; Golombek and McGill, 1983). On the Moon the mechanical discontinuity is assumed to be the megaregolith (Golombek, 1979; Golombek and McGill, 1983). An alternative kinematic model involves the development of a master fault that triggers the formation of the secondary antithetic fault (Melosh and Williams, 1989). In this model the initial fault is the major factor controlling graben width. Finite element modeling suggests that the presence of mechanical discontinuities has only a small effect on the width of the graben (Melosh and Williams, 1989). The master fault

Table 4.2 *Dimensions of lunar arcuate and linear rilles or graben*

Index	Latitude	Longitude	Maximum Depth (m)	Maximum Width (km)	Length (km)	D $\theta = 60°$ (m)
Brackett	17.5°N	23.2°E	230	1.71	93	266
Tetrazzini	26°N	0.6°W	140	5.0	50	162
Patricia	24.8°N	0.5°E	100	1.4	10	115
Bradley	24°N	1°W	400	3.25	127	462
Alphonsus	13°S	1.8°W	120	0.8	51	139
Littrow	22.2°N	29.4°E	280	2.25	34	323

Depth and dimensions were determined using Lunar Topographic Orthophotomaps (LTOs).

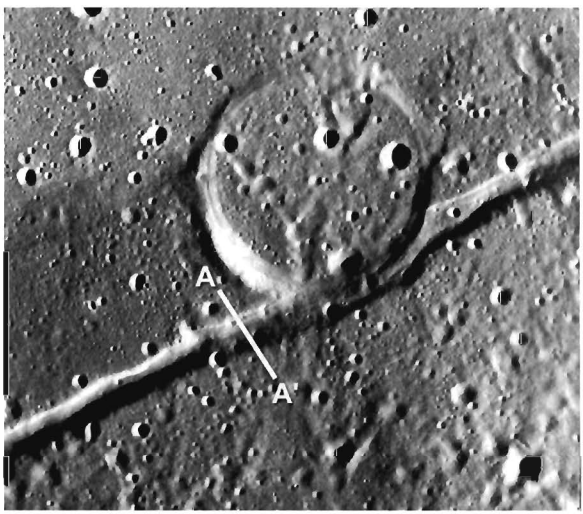

Figure 4.14. Brackett graben of Fossae Plinius (17.8°N, 23.5°E). Brackett is an arcuate graben on the southern margin of Mare Serenitatis (Panoramic Camera frame AS17-2331).

kinematic model is also supported by field studies of the graben in Canyonlands National Park (Moore and Schultz, 1999).

2.2.1 Topography of lunar graben

As with mare ridges, the best available topography for lunar graben is from Lunar Topographic Orthophotomaps. However, only a few lunar graben are covered by LTOs with sufficient resolution. The maximum relief of six lunar graben segments was measured (Table 4.2). The measured graben have a maximum relief that varies from about 100 to 400 m (mean ~210 m). The maximum width of these lunar graben ranges from about 800 m to 5 km (mean ~2.4 km). Profiles across the graben confirm that they are characterized by relatively steep walls and flat floors. A topographic profile across a prominent arcuate graben in southern Mare Serenitatis (a graben of Fossae Plinius) shows that it is relatively narrow (~1.7 km in width)

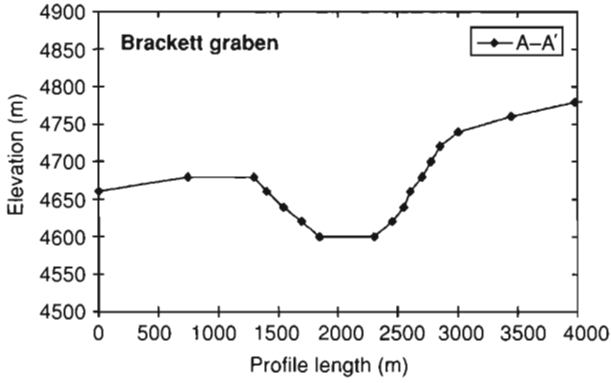

Figure 4.15. Topographic profile across Brackett indicates that the southern wall of the graben is offset relative to the northern wall. The topographic profile was constructed from a 1:50 000 LTO (42C4S1). Profile location is shown in Figure 4.14. Elevations are relative to an arbitrary zero vertical datum of 1 730 000 m.

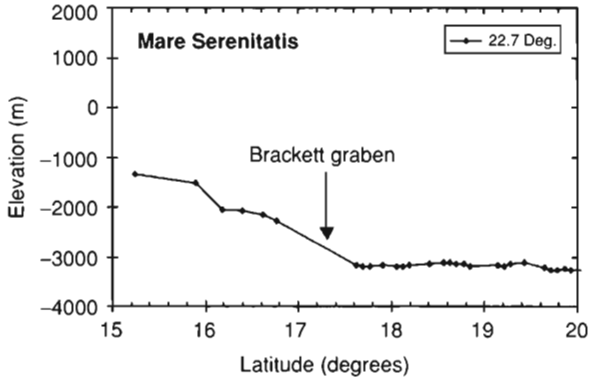

Figure 4.16. Clementine LIDAR profile located at approximately 22.7°E longitude crossing Brackett graben in Mare Serenitatis. The approximate location of Brackett graben is shown by the arrow. The LIDAR data were extracted from the dataset of Smith *et al.* (1997). Elevations are in meters above an ellipsoid of radius 1738 km at the equator with a flattening of 1/3234.93 corresponding to the flattening of the geoid. The vertical exaggeration is ~16:1.

with a flat floor (Figure 4.14). The graben appears to crosscut the southern end of Dorsum Nicol (Figure 4.5). The graben walls have relatively shallow maximum slopes ranging from ~8° to 12°. The topography also shows an offset across the graben of 60 m (Figure 4.15). This indicates that the graben is formed on a sloping mare surface, increasing in elevation to the south. Clementine LIDAR data show a rapid increase in elevation of the mare surface near the margins of Mare Serenatitis where arcuate graben of Fossae Plinius are located (see Plate 7, Figure 4.16). A topographic offset also occurs across an arcuate graben of Fossae Littrow, located

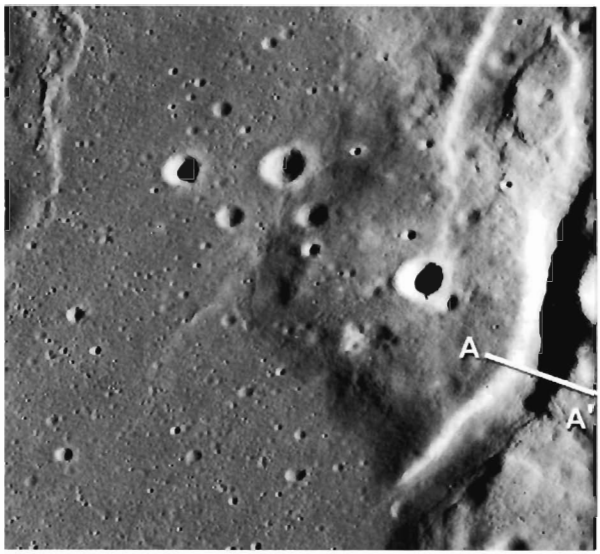

Figure 4.17. The Littrow graben of Fossae Littrow (22°N, 29.3°E) on the eastern margin of Mare Serenitatis. The Littrow graben abruptly terminates in the mare suggesting that it predates the emplacement of mare basalts that flooded the eastern margin of the basin (Panoramic Camera frame AS17-2313).

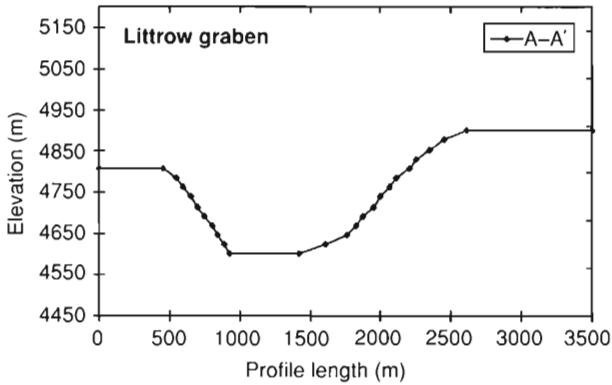

Figure 4.18. Topographic profile across the Littrow graben indicates an offset of the eastern wall relative to the western wall. The topographic profile was constructed from a 1:50 000 LTO (42C2S1). Profile location is shown in Figure 4.17. Elevations are relative to an arbitrary zero vertical datum of 1 730 000 m.

on the eastern margin of Mare Serenatitis (Figure 4.17). The Littrow graben has a maximum measured relief of ~280 m, and a maximum width of ~2.3 km. The walls of the Littrow graben are steeper than the Plinius graben slopes, ranging from ~16° to 23°, and the elevation offset across the structure is 80 m (Figure 4.18). Of the lunar graben examined (Table 4.2), most that are circumferential to mare basins exhibit elevation offsets (e.g., Plinius, Littrow, Tetrazzini). The longest and deepest of the graben examined is Fossa Bradley (Table 4.2). Bradley is a linear graben, circumferential to Mare Imbrium and exhibits no significant elevation offset.

2.2.2 Crater floor graben

Graben and fractures in the floors of impact craters are common lunar tectonic structures (Schultz, 1976b; Wilhelms, 1987). Often these graben form a rough polygonal pattern. Examples are the graben of Fossae Alphonsus that occur in the floor material of the Alphonsus impact crater located near the edge of Mare Nubium (Carr, 1969; McCauley, 1969). This 115 km diameter highland crater was the site of impact of Ranger 9 (see McCauley, 1969). Topographic profiles across a graben of Fossae Alphonsus, the narrowest of the graben examined, indicate no elevation offset (Table 4.2). It is generally agreed that uplift of the crater floor is the source of the stresses that form the graben and fractures. The fractured floor material is often at a higher elevation relative to the rims than the floors of craters without fractures (Pike, 1971; Wilhelms, 1987). The cause of the uplift, however, is not completely clear. Uplift and subsequent faulting of the crater floor material may have resulted from viscous relaxation (Hall *et al.*, 1981). Alternatively, uplift may result from igneous intrusions since many of the floor-fractured craters occur near maria (Brennan, 1975; Schultz, 1976b; Wichman and Schultz, 1995). Dombard and Gillis (2001) used finite element analysis to model elastoviscoplastic deformation of a reasonable analogue to lunar crustal materials and concluded that topographic relaxation cannot account for the majority of floor-fractured craters (diameters less than ~60 km). Thus, they favor igneous intrusion over relaxation.

2.2.3 Rupes Recta normal fault

The vast majority of the extensional landforms on the Moon are troughs, clearly reflecting a set of graben-forming antithetic normal faults. There are, however, rare cases of extension involving a single normal fault expressed as a scarp. The best example is Rupes Recta, commonly called the "Straight Wall." Located in Mare Nubium, it casts a prominent shadow on the mare surface during the lunar sunrise, making it a favorite among amateur astronomers. Rupes Recta is generally linear over much of its ~112 km length (Figure 4.19). The fault cuts mare basalts that partially flooded a pre-Nectarian crater on the southeastern edge of Nubium. Wrinkle ridges appear to outline the western half of this ancient crater; the buried rim likely localized the mare ridges (Plate 6A). The most curvilinear section of the scarp is near its southern terminus. This is also where the Rupes Recta normal fault extends from the Nubium mare basalts into an embayed inlier of highlands material (Figure 4.19). Also remarkable is the lack of segmentation of the fault. There is only one clear fault segment; the southernmost segment where the fault is the most curvilinear. Other segment boundaries may be marked by several slump blocks along the scarp wall. The elevation of the Rupes Recta has been estimated from shadow measurement to be a maximum of ~300 m. Clementine LIDAR data across

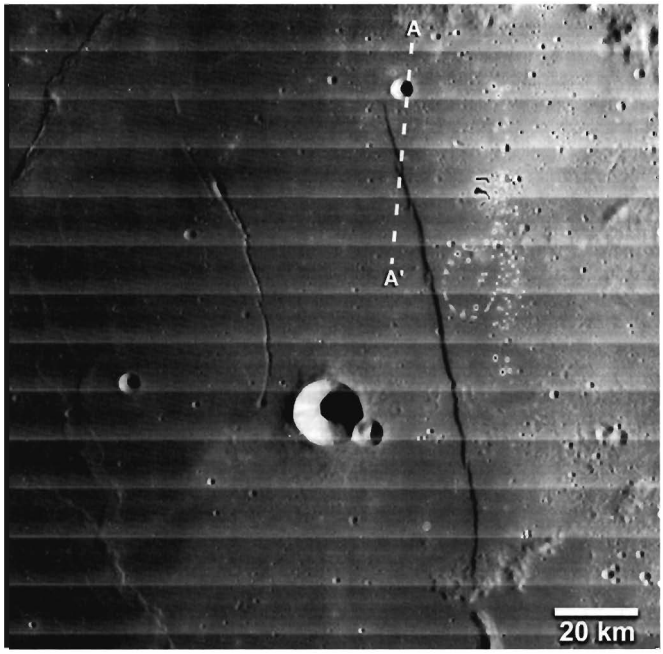

Figure 4.19. Rupes Recta located in southeastern Mare Nubium. The scarp, commonly known as the "Straight Wall," is the surface expression of a normal fault (mosaic of Lunar Orbiter frames IV-133-H1, H2).

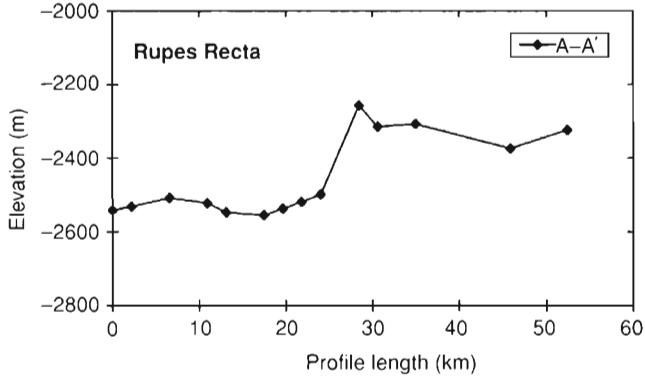

Figure 4.20. Clementine LIDAR profile crossing Rupes Recta. The LIDAR data were extracted from the dataset of Smith *et al.* (1997). Elevations are in meters above an ellipsoid of radius 1738 km at the equator with a flattening of 1/3234.93 corresponding to the flattening of the geoid. Profile location is shown in Figure 4.19. The vertical exaggeration is 48:1.

the northern section of Rupes Recta indicates a maximum relief of ~240 m at this location (Figure 4.20). The Clementine orbit track crosses Rupes Recta at an acute angle (Figure 4.19) and traverses one of the slump blocks along the wall. Thus, the slope at this location cannot be accurately measured from the LIDAR profile. However, with a measured relief of ~240 m and a scarp face width of ~600 m (measured from a Clementine 750 nm mosaic), the maximum slope at this location

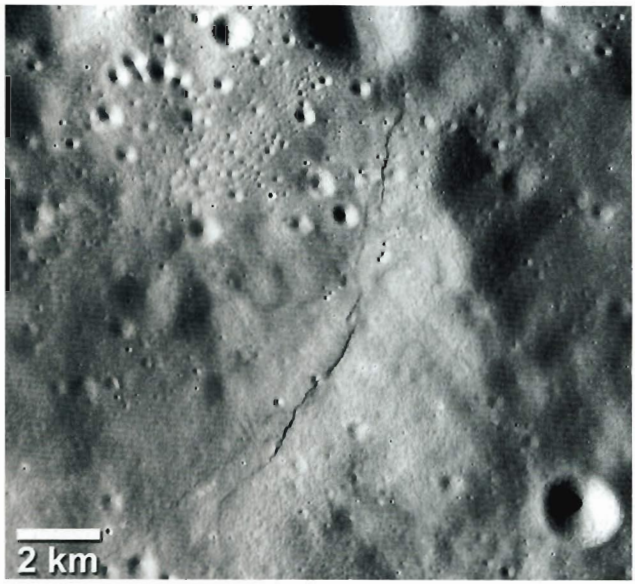

Figure 4.21. Lobate scarp in the farside highlands (6.8°N, 129.7°E). This series of en-echelon stepping lobate scarps, also referred to as Morozov scarp for a nearby crater (Binder and Gunga, 1985), has an estimated maximum relief of ~20 m and a combined length of ~10 km. The scarp cuts a small impact crater suggesting it is the surface expression of a thrust fault (Panoramic Camera frame AS16-4970).

is >20°. This is in the upper range of slopes measured on lunar graben walls (see Section 2.2.1). The LIDAR profile also shows that the scarp is flanked by a rise (Figure 4.20). The presence of the rise is subtly expressed in high-resolution Lunar Orbiter images of Rupes Recta. Flanking topographic rises are also associated with graben in the Caloris basin on Mercury (see Watters and Nimmo, Chapter 2).

The Rupes Recta normal fault appears to be relatively young. Because the fault offsets the floor of Mare Nubium, it clearly postdates the emplacement of the mare basalts. A young age is also suggested by the fact that the fault cuts and offsets the rim walls of two small impact craters (Figure 4.19). The larger of the two craters is ~2 km in diameter. No craters of this diameter or larger are superposed on the fault scarp.

2.3 Lunar scarps

Unlike the other major tectonic features of the Moon, the lunar lobate scarps were not detected in Earth-based telescopic surveys. This is because lunar scarps are generally small-scale structures compared to many mare ridges and rilles. In fact, most lunar scarps are only easily resolved in the highest resolution images of the lunar surface, acquired by the Apollo Panoramic Cameras (Mattingly *et al.*, 1972; Schultz, 1976a; Masursky *et al.*, 1978). In a survey of the lunar highlands using Apollo 15, 16 and some 17 Panoramic Camera images, Binder and Gunga (1985) found a total of 71 scarps. They grouped these features into three broad morphologic classes: linear, arcuate, and irregular. Many of the scarps consist of a series of

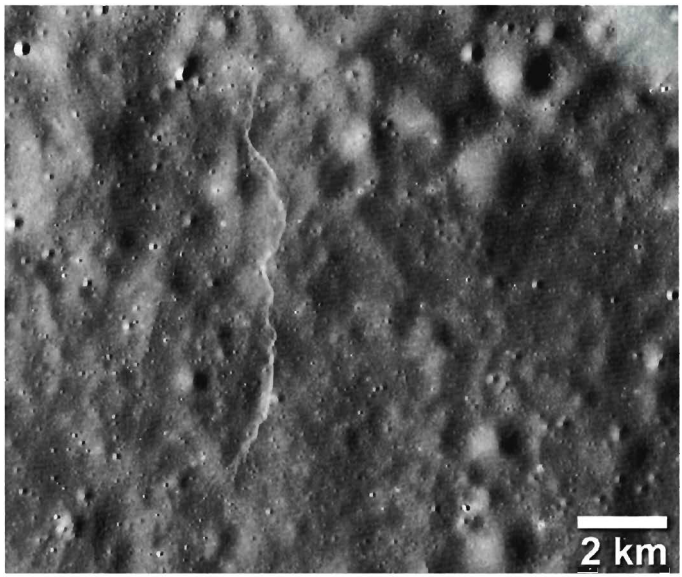

Figure 4.22. Lobate scarp segment in series that cut Mandel'shtam crater in the farside highlands (6.9°N, 161.5°E). The scarp is lobate with a relatively steeply sloping scarp face and a gently sloping back scarp (Panoramic camera frame AS16-4150).

en-echelon stepping segments (Figure 4.21). Other scarps occur in clusters that cover relatively small areas, and the scarps are closely spaced and exhibit parallel to subparallel orientations (Binder and Gunga, 1985, Fig. 7). Lunar scarps are often lobate, one-sided structures with a relatively steeply sloping scarp face and a gently sloping back scarp (Figure 4.22). The lobate nature of many lunar scarps led the Apollo 16 astronauts to describe them as having the appearance of flow fronts (Mattingly *et al.*, 1972). They also noted reversals in the direction of the scarp face along strike. Reversals in vergence of en-echelon stepping scarps is a common characteristic of planetary lobate scarp thrust faults (Watters and Nimmo, Chapter 2; Golombek and Phillips, Chapter 5). Many of the identified lobate scarps occur in the lunar highlands (Plates 6A,B) and are thus often referred to as "highland scarps". However, some lobate scarps are found in mare basalts, specifically in Mare Nectaris, Mare Cognitum, and Mare Serenitatis (Plate 6A).

2.3.1 Topography of lunar scarps

The resolution of nearly all the currently available topographic data for the Moon is too low to characterize lunar lobate scarps. Only topography derived from Panoramic Camera stereo pairs has sufficient spatial and vertical resolution. Such high resolution topographic maps were generated for the Apollo landing sites.

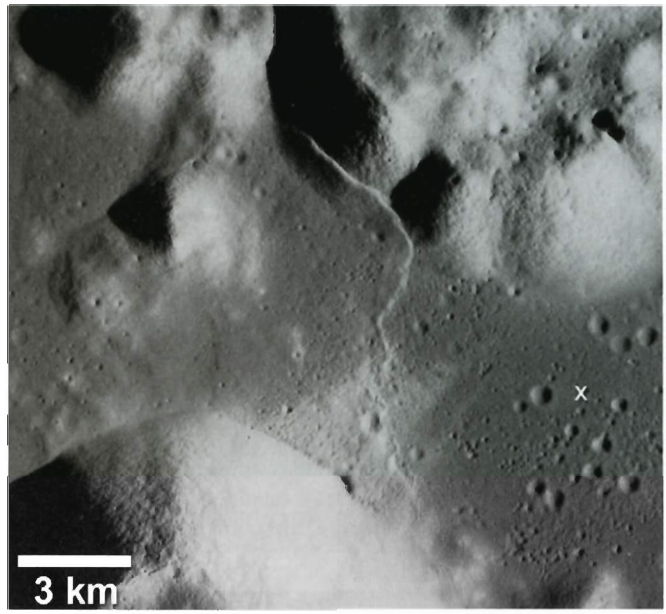

Figure 4.23. Lee-Lincoln scarps in the Tauras-Littrow valley. The Lee-Lincoln thrust fault scarp cuts across the mare basalt floor of the Tauras-Littrow valley and extends up onto the highlands of North Massif. This fault scarp was examined and traversed by the Apollo 17 astronauts Eugene A. Cernan and Harrison H. Schmitt. The "X" marks the approximate location of the Apollo 17 landing site (Panoramic camera frame AS17-2309).

The Apollo 17 landing site is located in the Tauras-Littrow Valley on the south-eastern margin of Mare Seneratitis. The Lee-Lincoln scarp cuts the floor of the Tauras-Littrow Valley, trending roughly north–south between the South Massif and North Massif (Schmitt and Cernan, 1973; Scott, 1973). The scarp extends into the highlands of the North Massif, cutting upslope, but abruptly changes trend to the northwest, cutting along slope (Figure 4.23). There are two special scale topographic maps of the Tauras-Littrow Valley, a 1:25 000 scale LTO and a 1:50 000 scale U.S. Geologic Survey map (USGS, 1972). Robinson and Jolliff (2002) generated a DEM of the Tauras-Littrow Valley using the USGS map (Plate 8). The Lee-Lincoln scarp has the greatest relief (~80 m) in the Tauras-Littrow Valley where the thrust fault offsets the mare basalts that make up the floor of the valley (Plate 8). The relief of the scarp in the highlands is markedly less than the maximum reached in the valley. The largest measured slope on the scarp face is ~27° and occurs in the valley on the southern section of the scarp, near the South Massif. Just before the Apollo 17 astronauts started up the slopes of the southern section of the Lee-Lincoln scarp in the LRV, Harrison Schmitt described the scarp as very rolling and relatively smooth with no exposed outcrops. The maximum slope of the scarp face near where Cernan and Schmitt traversed the scarp is ~20°.

In an effort to estimate the relief of other lunar lobate scarps, shadow measurements were made on scarp segments near the craters Madler A and Morozov. Portions of Panoramic Camera images (second generation positive film transparencies) were scanned at high resolution and shadows were measured from the digital

Table 4.3 *Dimensions of lobate scarps on the Moon*

Index	Latitude	Longitude	Maximum Relief (m)	Length (km)	D $\theta = 30°$, (m)
Madler S1	10.8°S	31.8°E	53	1.75	106
Madler S2	10.8°S	31.75°E	25	1.58	50
Madler S3	10.7°S	31.5°E	54	7.77	108
Madler S4	10.6°S	31.45°E	38	4.94	76
Morozov S1	6.76°N	129.68°E	17	5.72	34
Morozov S2	6.85°N	129.73°E	7	0.72	14
Morozov S3	6.95°N	129.75°E	6	1.25	12
Morozov S4	6.99°N	129.75°E	10	1.78	20
Lee-Lincoln	20.27°N	30.56°E	80	13.86	160

Relief was determined using shadow measurements made on Apollo Panoramic camera images with the exception of Lee-Lincoln. Relief on the Lee-Lincoln scarp was determined from a digital elevation model (DEM) of the Taurus-Littrow Valley (see Plate 7).

images. The estimated maximum relief of the scarps measured varies from 6 ± 2 to 54 ± 2 m ($n = 8$) (Table 4.3). The mean maximum relief of all the scarps measured (including the Lee-Lincoln scarp) is ~32 m ($n = 9$).

2.4 Wrinkle ridge – lobate scarp transitions

Mare ridges and lobate scarps have distinct differences in morphology. As described above, wrinkle ridges are complex structures that may have multiple superposed landforms. Lobate scarps, by contrast, are relatively simple structures morphologically, usually consisting of a relatively steep scarp face and a gently sloping back scarp. Both structures, however, are to some degree surface manifestations of thrust faults and are thus related tectonic landforms. This relationship is clearly demonstrated by wrinkle ridge – lobate scarp transitions. A prominent example is found on the eastern edge of Oceanus Procellarum where a mare ridge extends to the Montes Riphaeus, which separates Procellarum and Mare Cognitum (Masursky *et al.*, 1978). In the highlands of Montes Riphaeus (~8°S, 28°W) the lobate scarp consists of both linear and lobate segments and has a rare subsidiary, flanking scarp (Figure 4.24). Although rare, multiple, flanking (or piggybacking) scarps are also found on Mercury (Watters and Nimmo, Chapter 2). The Montes Riphaeus scarp cuts directly across the highlands into Mare Cognitum. In Cognitum, the lobate scarp is expressed by a series of linear segments that appear to be localized at the contact between the mare and highlands (Figure 4.24) (see Masursky *et al.*, 1978). Some wrinkle ridge – scarp transitions are not located at the margins of mare basins. In the highlands south of Mare Australe (~53°S, 104°E), a lobate scarp transitions

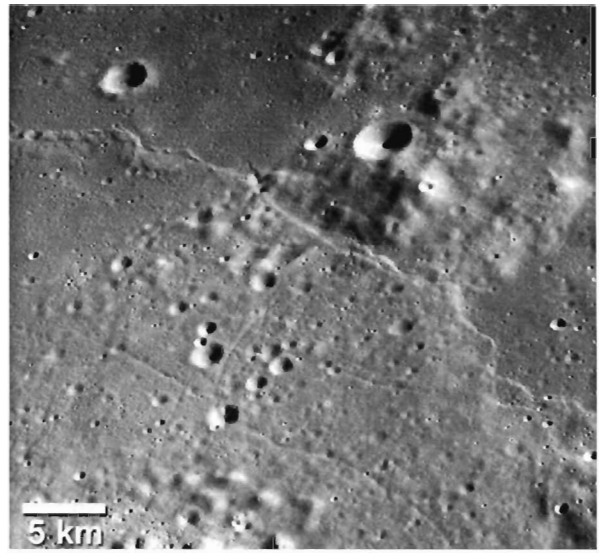

Figure 4.24. Wrinkle ridge – lobate scarp transition in the area of Montes Riphaeus between Mare Cognitium and Oceanus Procellarum. The lobate scarp cuts the highlands of Montes Riphaeus and has two distinct terraces in the central montes that may reflect imbricate thrust faulting (Panoramic Camera frame AS16-5452).

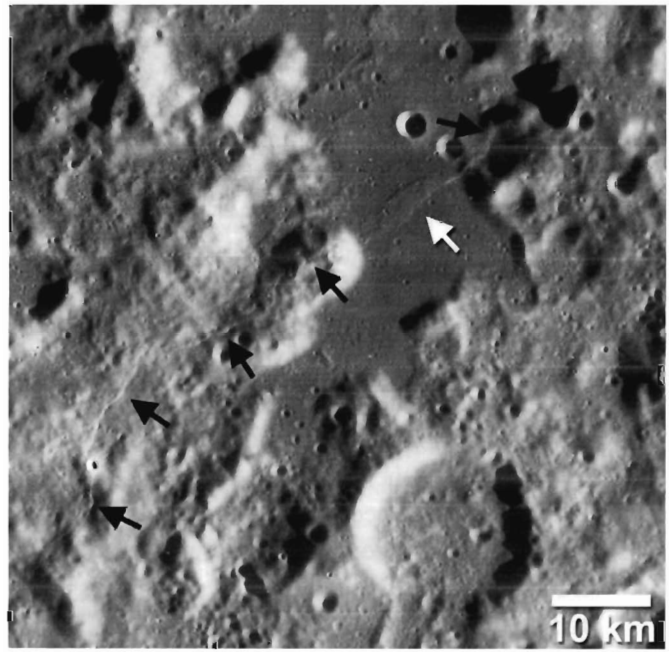

Figure 4.25. Lobate scarp in the highlands south of Mare Humorum. The northeast trending lobate scarp (left-pointing black arrows) extends across a small patch of mare basalts in the valley where it transitions into a wrinkle ridge (white arrow). The wrinkle ridge crosses the mare basalts to the highlands where the structure transitions back to a lobate scarp (right-pointing black arrow) and cuts across and along slope (Lunar Orbiter frame IV-136-H3).

to a mare ridge as the structure extends into the mare-filled Kugler crater (Schultz, 1976a; Raitala, 1984). A very similar ridge – scarp transition involving an impact crater filled with volcanic plains occurs on Mars in the area just northeast of the Herschel basin (Watters, 1993, Fig. 4b). One of the most unusual wrinkle ridge – lobate scarp transitions is found in the highlands south of Mare Humorum. Here a lobate scarp transitions into a wrinkle ridge where the structure crosses a small valley filled with mare basalts (Figure 4.25). The wrinkle ridge then transitions

back to a lobate scarp in the highlands to the north of the mare basalts, where the scarp cuts across and along slope.

There are other cases of wrinkle ridge – lobate scarp transitions on the Moon where the scarps parallel mare–highland contacts. One is associated with Dorsa Aldrovandi, located on the eastern margin of Mare Serenitatis (Figure 4.9) (see Howard and Muehlberger, 1973). As described previously (see subsection 2.1.2), segments of Dorsa Aldrovandi (like the Littrow ridge) have large elevation offsets from the basin-interior side to the margin side of the ridge segments. The northernmost segment of the ridge reaches the highlands at the basin margin. The structure, however, does not terminate at the contacts between the mare basalts and the highlands. The structure extends into the highlands as a lobate scarp, cutting along slope (Howard and Muehlberger, 1973, Figs. 31–33). This is also the case for a transition on the western margin of Mare Serenitatis, referred to by Lucchitta (1976) as the West Serenitatis scarp. As described in subsection 2.3.1, where the Lee-Lincoln scarp extends from the Taurus-Littrow valley into the North Massif, the scarp only cuts up slope for a short distance before its trend changes to the northwest, where it cuts along slope (Figure 4.23). Although the Lee-Lincoln scarp has been described as a wrinkle ridge – lobate scarp transition (Howard and Muehlberger, 1973; Lucchitta, 1976; Watters, 1988), only the southernmost segment (near South Massif) has some characteristics of wrinkle-ridge morphology. Much of the segment of the scarp in the mare basalts of the valley floor has the morphology of a lobate scarp (Figure 4.23). The fact that in some cases lobate scarp thrust faults do not cut across highland massifs but roughly parallel the contacts between the mare basalts and the highlands is an important constraint on the kinematics of their formation. Howard and Muehlberger (1973) suggested that the lobate scarp thrust faults are rooted in a decollement, formed at the base of the highlands regolith.

The change in deformation style between the mare basalts and the highlands material may be the result of a contrast in the mechanical properties of the materials (Watters, 1988), specifically the presence or absence of layering (Watters, 1991). Photogeologic evidence and radar sounder data (see subsection 2.1.4) suggest the mare basalts that flooded the nearside basins consist of a sequence of flows separated by interbeds. The highlands materials by contrast are generally mechanically isotropic (i.e. lacking layering). The presence of layering, however, may not result in a sufficient contrast in the mechanical properties. The strength of a multilayer is determined by the mechanical nature of the contacts between the layers (Johnson, 1980). A multilayer will have a greater tendency to deform by folding and faulting when the contacts between layers have low yield strengths (Johnson, 1980). For example, an upward propagating blind thrust fault will induce folding of a multilayer if the layer contacts are weak (Nino *et al.*, 1998). If on the other hand

the contacts are strong, faulting is favored and the fault is expected to propagate through the sequence and become surface-breaking (Roering *et al.*, 1997; Nino *et al.*, 1998). Since lobate scarps appear to form over surface-breaking thrust faults, if there is layering in the lunar highlands the contacts must be strong and resist slip. In mare basalt sequences, slip between layers probably occurred in interbeds with low shear strengths (see Watters, 1991).

2.5 Displacement–length relationships of lunar tectonic features

It has been shown that the maximum displacement D on a fault scales with the planimetric length L of the fault (e.g., Walsh and Watterson, 1988; Cowie and Scholz, 1992a,b; Gillespie *et al.*, 1992; Cartwright *et al.*, 1995). The scaling relationship applies to normal, strike-slip, and thrust faults found in a wide variety of terrestrial tectonic settings and over eight orders of magnitude in length scale (Cowie and Scholz, 1992b). Planetary faults also exhibit this scaling relationship (Schultz and Fori, 1996; Schultz, 1997, 1999; Schultz *et al.*, Chapter 10; Watters and Robinson, 1999; Watters *et al.*, 1998, 2000; Watters, 2003). The displacement, D, is related to fault length, L, by $D = cL^n$, where c is a constant related to material properties and n is estimated to be >1 (Walsh and Watterson, 1988; Marrett and Allmendinger, 1991; Gillespie *et al.*, 1992). Studies of terrestrial fault populations formed in uniform rock types suggest the relationship $D = \gamma L$ is linear, where the ratio γ is a constant determined by rock type and tectonic setting (for $n = 1$, $\gamma = c$) (Dawers *et al.*, 1993; Clark and Cox, 1996; Hardacre and Cowie, 2003). Cowie and Scholz (1992a) suggest that γ reflects the mechanical properties of the rock and the regional stresses. The values of γ for the fault populations analyzed by Cowie and Scholz (1992b) range from 10^0 and 10^{-3}. Fault segmentation, uncertainties in fault dip and depth or aspect ratio, interaction with other faults, and ambiguities in determining the maximum value of D along the scarp trace are possible sources of scatter in the D–L data (Cartwright *et al.*, 1995, 1996; Dawers and Anders, 1995; Wojtal, 1996; Schultz, 1999).

Assuming the maximum relief h of the wrinkle ridge is a function of the total slip on the underlying thrust fault and the dip of the fault plane θ, the displacement can be estimated by $D = h/\sin\theta$ (see Wojtal, 1996; Watters *et al.*, 2000). This approach assumes that the bulk of the horizontal shortening is due to displacement on thrust faults and does not account for the component of shortening due to folding (see Watters, 1988; Golombek *et al.*, 1991). The displacement on mare ridge thrust faults is estimated to range from 100 to 820 m with an average of ~510 m ($n = 12$), assuming fault plane dips of 30° (Table 4.1). A linear fit to the D–L data for the mare ridges yields a value of $\gamma \cong 6.5 \times 10^{-3}$ for $\theta = 30°$. This is consistent with estimates of γ for Mercury wrinkle ridges (~3.5×10^{-3} for $\theta = 30°$) (Watters and

Nimmo, Chapter 2). Estimates of γ for analogue structures on the Columbia Plateau (Watters, 1988, 1992) are $2.9 \pm 1.0 \times 10^{-2}$ larger (Mege and Reidel, 2001), likely due to the much larger accumulated shortening on the anticlinal ridges (Reidel, 1984).

The *D–L* relationship for lunar graben can be determined from the available topography (Table 4.2) if the fault plane dips are known. The slopes of the measured graben walls do not exceed 25° (see preceding section), which is much lower than likely fault plane dips on the bounding normal faults (>45°). The low slopes of the bounding walls are not unique to lunar graben. The walls of graben in the Caloris basin on Mercury also have low slopes (Watters and Nimmo, Chapter 2), and are likely the result of mass wasting related to impact processes. Thus, the fault plane dips of the bounding normal faults were probably much higher than the current slopes of the graben walls.

It has been observed that the width of lunar graben increases with increasing elevation (McGill, 1971; Golombek, 1979). This relationship can be used to estimate the fault plane dip θ using a two point method

$$\tan\theta = 2\Delta E/(W_u - W_l), \tag{4.1}$$

where ΔE is the change in elevation and W_u and W_l are the widths of the graben at the high- and low-elevation points, respectively (McGill, 1971; Golombek, 1979). It is assumed that the bounding faults have roughly equal (and constant along their length) dips and that the faults intersect at a constant depth. A variation of the two point method uses the slope of a linear least-squares fit to a plot of width versus elevation along the lengths of lunar graben to estimate the average dips of the bounding faults (McGill, 1971; Golombek, 1979). McGill (1971) and Golombek (1979) examined a total of 19 lunar graben and reported fault plane dips with a mean of 61°. The large variation in average dip yielded by the linear regression method led to the conclusion that the bounding faults do not have a constant depth of intersection along their lengths (Golombek, 1979).

Assuming the fault plane dips of the bounding faults of lunar graben are ~60°, the estimated displacement on the normal faults ranges from 0.12 to 0.46 km with an average of ~0.24 km ($n = 6$) (Table 4.2). A linear fit to the *D–L* data for the graben yields a value of $\gamma \cong 3.6 \times 10^{-3}$ ($\theta = 60°$). The range of displacements and γ for the lunar graben are in good agreement with those determined for graben in the Caloris basin on Mercury ($\gamma \cong 2.2 \times 10^{-3}$ for $\theta = 60°$) (Watters *et al.*, 2005; Watters and Nimmo, Chapter 2).

An accurate estimate of the *D–L* ratio for lobate scarp thrust faults on the Moon is more challenging because of their scale. Using estimates of the maximum relief obtained from the available topography and shadow measurements, and

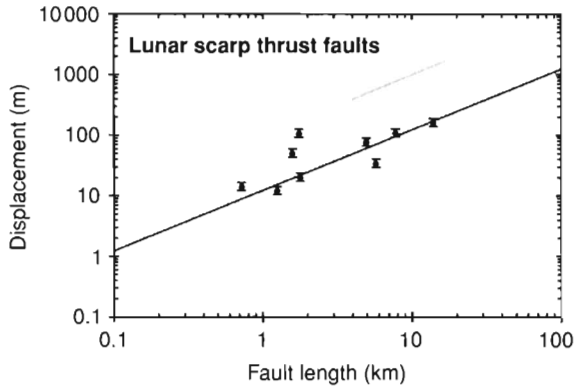

Figure 4.26. Log–log plot of maximum displacement as a function of fault length for nine lunar lobate scarp segments. The ratio γ ($\sim 1.2 \times 10^{-2}$ using estimates of D based on fault plane dips $\theta = 30°$) for the thrust faults (Table 4.3) were obtained by a linear fit to the D–L data with the intercept set to the origin (Cowie and Scholz, 1992b).

measurements of fault segment lengths, the displacement on lunar scarp thrust faults ranges from 12 to 160 m, assuming fault plane dips $\theta = 30°$ (Table 4.3) with a mean of ~64 m ($n = 9$). Lengths of the measured scarp segments range from ~0.72 to 13.9 km with a mean of ~4.4 km. The value of γ, determined from a linear fit to the D–L data for the lunar lobate scarps, for a range in θ of 25° to 35° is $\sim 1.5 \times 10^{-2}$ to $\sim 1.1 \times 10^{-2}$ and $\gamma \cong 1.2 \times 10^{-2}$ for $\theta = 30°$ (Figure 4.26). This range of γ is larger than estimates of γ for larger scale lobate scarp populations on Mercury and Mars ($\sim 6.9 \times 10^{-3}$ and 6.2×10^{-3} respectively for $\theta = 30°$) (Watters, 2003; Watters and Nimmo, Chapter 2), but less than the γ for terrestrial thrust faults ($\sim 8.0 \times 10^{-2}$) (Watters *et al.*, 2000). Thus, the estimated γ for lunar lobate scarps is intermediate between that of lobate scarp thrust faults on Mercury and Mars and terrestrial thrust faults.

A likely explanation for the higher value of γ for terrestrial thrust faults compared to those on the Moon, Mercury and Mars is the friction on the faults (see Watters and Nimmo, Chapter 2; Schultz *et al.*, Chapter 10). The presence of water on Earth lubricates faults, effectively reducing the residual frictional stress σ_f on the faults. The absence of water is thus expected to result in higher values of σ_f on the Moon and Mercury and stronger faults. The similar values of γ for thrust faults on Mercury and Mars suggest the first-order mechanical properties of intercrater plains on the two planets are similar (Watters *et al.*, 2000) and also suggest that water was not abundant in the Martian cratered highlands at the time the thrust faults formed.

3 Timing of wrinkle-ridge, graben, and lobate scarp formation

The age of wrinkle-ridge and graben formation is critical to understanding the evolution of tectonic stresses on the Moon. The age of these tectonic features can be constrained by determining the age of the geologic units they deform. Unlike other planetary surfaces, the ages of geologic units based on crater counts, particularly some mare basalts, can be calibrated in absolute age by radiometric dating of lunar rock samples returned in the Apollo and Luna missions (see Wilhelms, 1987; Neukum and Ivanov, 1994; Stöffler and Ryder, 2001; Hiesinger *et al.*, 2000, 2003).

In an effort to characterize the superposition relationship of linear and arcuate rilles on the nearside, Lucchitta and Watkins (1978) determined that 64% of the combined length of the graben (17 000 km) occurs in highlands, highland plains, and Imbrian crater material, and 35% occurs in mare units (see Plates 9A,B). The large cumulative length of graben superposed on mare units and highland plains material indicates that graben postdate the formation of the nearside impact basins and the emplacement of the mare basalts. This is supported by the strong spatial and azimuthal correlation between linear and arcuate graben and the mare basins (Plate 6A), and the absence of graben on the farside outside of Orientale basin material (Plate 9B). There is no evidence that the observed graben formed before the end of the period of heavy bombardment (Lucchitta and Watkins, 1978). This does not preclude the possibility that extension of the lunar crust occurred before or during the period of heavy bombardment, since no record of these faults would be expected to be preserved. Examination of the superposition relationships of graben that occur in mare basalts suggests that they are restricted to relatively old mare units surrounding Serenitatis, Tranquillitatis and Humorum (Boyce, 1976; Lucchitta and Watkins, 1978) (Plate 9A). Crater density ages of the mare units indicated that no mare basalts younger than $\sim 3.6 \pm 0.2$ Ga are cut by graben (Boyce, 1976; Lucchitta and Watkins, 1978). This is consistent with more recent crater density age estimates of the nearside mare basalts (Hiesinger *et al.*, 2000, 2003). Thus, crustal extension associated with lunar maria appears to have ceased at ~3.6 Ga.

Crustal shortening responsible for wrinkle-ridge formation in the mare basalts was much longer lived. Recent crater density age estimates by Hiesinger *et al.* (2000, 2003) suggest that basalt volcanism in nearside mare initiated ~4 Ga. The largest pulse of mare volcanism occurred in the Late Imbrian period that ended about 3.2 Ga (see Tanaka *et al.*, Chapter 8, Fig. 8.1). Lesser volumes of mare basalt were emplaced during the Eratosthenian and Copernican periods (Hiesinger *et al.*, 2000, 2003). The youngest mare basalt units occur in Oceanus Procellarum, embaying the southern portions of the Aristarchus plateau. The basalts are estimated to be ~1.2 Ga old (Hiesinger *et al.*, 2003). Wrinkle

ridges deform these relatively young mare basalts as well as the oldest mare units on the nearside in Mare Serenitatis, Mare Tranquillitatis, and Mare Nubium (Plate 9A). Thus, crustal shortening associated with lunar mare occurred as recently as ~1.2 Ga.

The timing of wrinkle-ridge formation can be further constrained by the relationship between structural relief and emplacement of the mare basalts. Evidence of ponded flows on mare ridges suggests that structural relief developed simultaneously with and following the emplacement of the mare basalts (Bryan, 1973; Schaber, 1973a,b; Schaber *et al.*, 1976). The greatest relief on the wrinkle ridges appears to have developed after the emplacement of the mare basalts ceased. A similar relationship between emplacement history and structural relief has been observed with anticlinal ridges of the Columbia Plateau (Watters, 1988) (see Section 2.1). Flows of the Columbia River Basalts Plateau are embayed by, and thin or pinch out on the flanks of the anticlines. Buckling was simultaneous with the emplacement of the oldest basalt flows and structural relief from cumulative displacement on thrust faults, and increased fold amplification was repeatedly buried by younger basalt flows (Reidel, 1984). Subsequent to the emplacement of the youngest flow, structural and topographic relief developed together. Thus, as is the case of the Columbia anticlinal ridges, deformation on mare ridges likely increases with depth and age. This suggests a long history of contractional deformation of mare basalts that is closely correlated spatially and temporally with the volcanic flooding of the maria.

The early termination of mascon-related extension and the subsequent dominance of compression in the maria until ~1.2 Ga suggest a compressional stress bias in the lunar lithosphere after ~3.6 Ga. The cessation of extension has been suggested to result from the superposition of compressional stresses from global contraction on flexural extensional stress due to loading by the mare basalts (Solomon and Head, 1979, 1980). This may have marked a stage in the Moon's thermal history around 3.6 Ga where interior cooling resulted in a shift from net expansion to net contraction (Solomon and Head, 1980).

Among the youngest lunar tectonic landforms are the lobate scarps. In fact, they may be some of the youngest endogenic features on the Moon. Schultz (1976a) first noted that the scarps were expressions of very young thrust faults. The age of the lobate scarps has been estimated by Binder and Gunga (1985) to be less than 1 Ga old. A young age for the scarps is supported by their relatively undegraded appearance and the absence of superimposed impact craters (see Figures 4.21, 4.22). Young lobate scarp thrust faults have been cited as evidence to support a late-stage compressional stress bias in the lunar lithosphere. Their young appearance raises the intriguing possibility that some of the lobate scarp thrust faults may be currently active.

4 Lunar seismicity

The Apollo seismic "network" comprised four stations at Apollo sites 12, 14, 15, and 16, forming a roughly triangular array with stations 12 and 14 at one corner, and stations 15 and 16 each about 1100 km away. Each station included a 3-component long-period seismometer and a single, vertical-component short-period seismometer (Lammlein *et al.*, 1974). The passive seismic experiment recorded data from 1969 until 1977, and 12 558 events were documented in the lunar event catalogue (Nakamura *et al.*, 1981). Recorded events exhibit different signal characteristics, and about 3000 of the catalogued events were classified as being from four types of sources: artificial impacts (8 events), meteoroid impacts (~1700 events), shallow moonquakes (28 events), and deep moonquakes (1360 events noted in the catalogue of Nakamura *et al.*, 1981). In addition, the thermal signature of the lunar sunrise and sunset is evidenced in the records (see, for example, Fig. 3 of Bulow *et al.*, 2005). Event identification and classification was originally made by eye, using hard copy print-outs and overlays of the seismograms recorded at Apollo stations 12, 14, 15, and 16.

Lunar seismicity provides information on the current state of the Moon's interior. Naturally occurring moonquakes indicate that there are locations or regions that are undergoing brittle failure in response to imposed stresses. Understanding the sources of the imposed stresses, and why certain regions can undergo failure, is important to establishing the present-day tectonic state of the Moon. Insofar as it is possible to estimate stress drops from the Apollo-era seismograms, these provide constraints on the energy release associated with moonquakes. Body-wave arrival times (i.e., P- and S-wave arrivals) recorded at multiple stations for a given moonquake allow the location of the quake to be determined, and simultaneously provide information (albeit limited) on the seismic velocity structure of the lunar interior. Seismic velocities in turn constrain elastic properties, which are controlled by temperature and composition.

There have been numerous investigations of lunar seismicity; recent reviews can be found in Wieczorek *et al.* (2006) and Lognonné and Johnson (2007). In this chapter we focus on the aspects of moonquakes that may, directly or indirectly, shed light on present and past lunar tectonics. We begin by examining the temporal and spatial occurrence of shallow and deep moonquakes, along with inferences regarding quake magnitudes and stress drops.

Interpretation of the Apollo seismic data is difficult for two main reasons. The first is the nature of the seismic station array – there are only three geographically distinct stations, and sensitivity to events is limited to an aperture extending beyond the array by approximately ~1100 km. Clearly then, recorded events will be biased to those occurring on the nearside, and this is evidenced in the data. The second difficulty is the low signal-to-noise of events seen in the seismograms

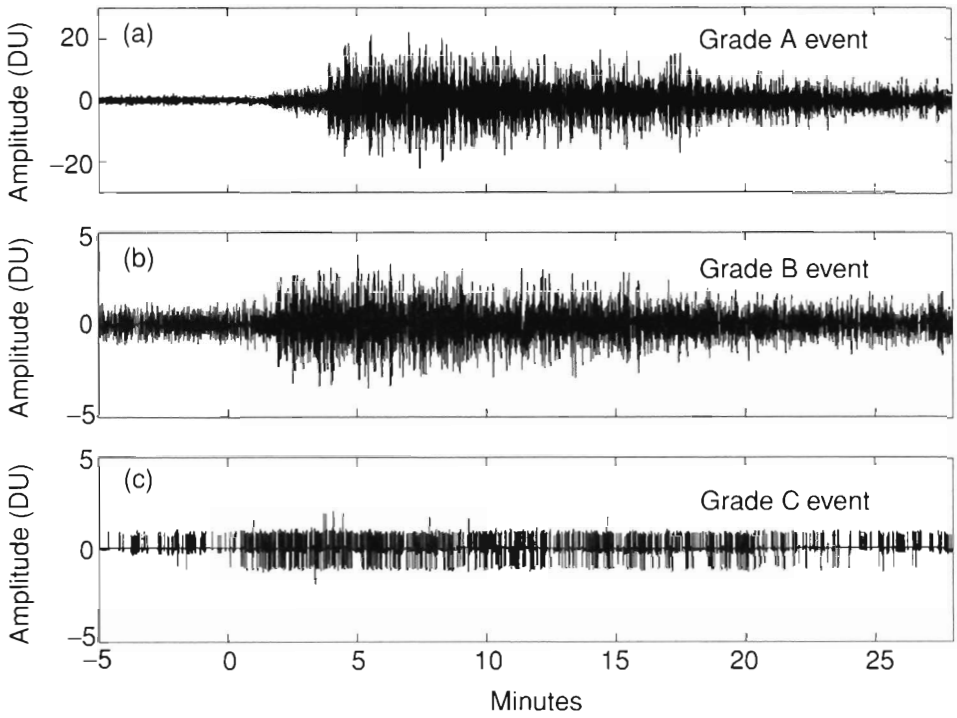

Figure 4.27. Typical data quality, as measured by visual inspection of the seismograms, of events in the lunar catalogue (Nakamura *et al.*, 1981). Waveform amplitudes are in digital units (DU). Approximately 2% of events have quality comparable to that in (a), 8% comparable to that in (b), and 57% comparable to that in (c). The remaining 33% are of poorer quality than that in (c). Figure taken from Bulow *et al.* (2005).

(Figure 4.27), and this is the combined result of several factors: (a) the limited dynamic range offered by the 10-bit instruments used, (b) the small magnitudes of most lunar events, and (c) long coda (i.e., seismic energy arriving long after the event itself) resulting from scattering in the lunar regolith. Consequently, identification of seismic phases in the seismograms is restricted to first arrivals of P and S waves; ideally these should be observed on as many stations as possible for successful determination of the moonquake location. This is often not the case, contributing to considerable uncertainty in the discussion of geographical variations in lunar seismicity.

4.1 Deep moonquakes

Among the first inferences from observations of the lunar seismic data was that some moonquakes tend to occur with tidal periods (Ewing *et al.*, 1971). Investigations revealed this population of quakes to have waveform characteristics that enabled them to be identified as distinct from other seismic events, such as meteorite

impacts (Lammlein, 1973; Lammlein *et al.*, 1974; Lammlein, 1977). Furthermore, it was found that subsets of the population exhibit similar waveforms – originally observed by overlaying seismogram traces, and now quantifiable through digital waveform cross-correlation (Nakamura, 2003, 2005; Bulow *et al.*, 2005, 2007). These observations, together with P- and S-wave arrival times, suggested that the quakes originate from deep (~800 to 1000 km) source regions that undergo repeated failure, giving rise to sets of moonquakes with similar waveforms and periodic occurrence times (Lammlein *et al.*, 1974). Despite the difficulties encountered in analyzing lunar seismic data, this first-order inference has stood the test of time.

Deep moonquakes have typical Richter magnitudes ~1, with the largest events having a magnitude ~3 and associated stress drops of about 10 kPa (Goins *et al.*, 1981). Such moonquakes are detectable due to the low seismic noise level on the Moon, specifically the absence of micro-seismic noise (Lognonné and Johnson, 2007). The waveform repeatability of deep moonquakes from a given source region has been of great help in both identification and classification of these events and in locating them. Typical seismograms for individual quakes from a given deep cluster are shown in Figure 4.28 – the low signal-to-noise ratio is apparent. However, seismograms for individual events from a given deep source region have coherent waveforms and so can be stacked, to enhance the signal-to-noise ratio (Figure 4.28). This has allowed a significant number of events to be added to the original 1360 deep moonquake population; the new additions are events that were either (a) previously identified but not recognizable as deep moonquakes (i.e., were listed as unclassified events in the original catalogue) or (b) not previously identified in the lunar seismograms (i.e., not in the original catalogue, even as an unclassified event). Nakamura (2003) used digital waveform cross-correlation, stacking, and single-link cluster analyses to classify many of the previously 9128 unclassified events in the lunar catalogue as deep moonquakes. His study has expanded the number of known deep moonquakes in the original catalogue to 7245, and has established that these events originate from at least 160 deep source regions. In a subsequent study, Nakamura (2005) established the locations of deep source regions with sufficient travel time picks – 98 can be located on the nearside, and 8 may be farside source regions. Bulow *et al.* (2005, 2007) used waveform coherence and stacking to produce a "target" waveform for a known deep source region, and then cross-correlated this target waveform with the entire continuous time series to search for previously unidentified events from that source region (see Bulow *et al.* (2005) for details of the approach). This has resulted in an average increase in the number of events at eight nearside deep source regions of 30%, with one region yielding a 50% increase in the number of events. All of these eight clusters contain at least 140 events, and the study of Bulow *et al.* (2007) contributes an additional 503 events to the 7245 events of Nakamura (2005). The most-studied

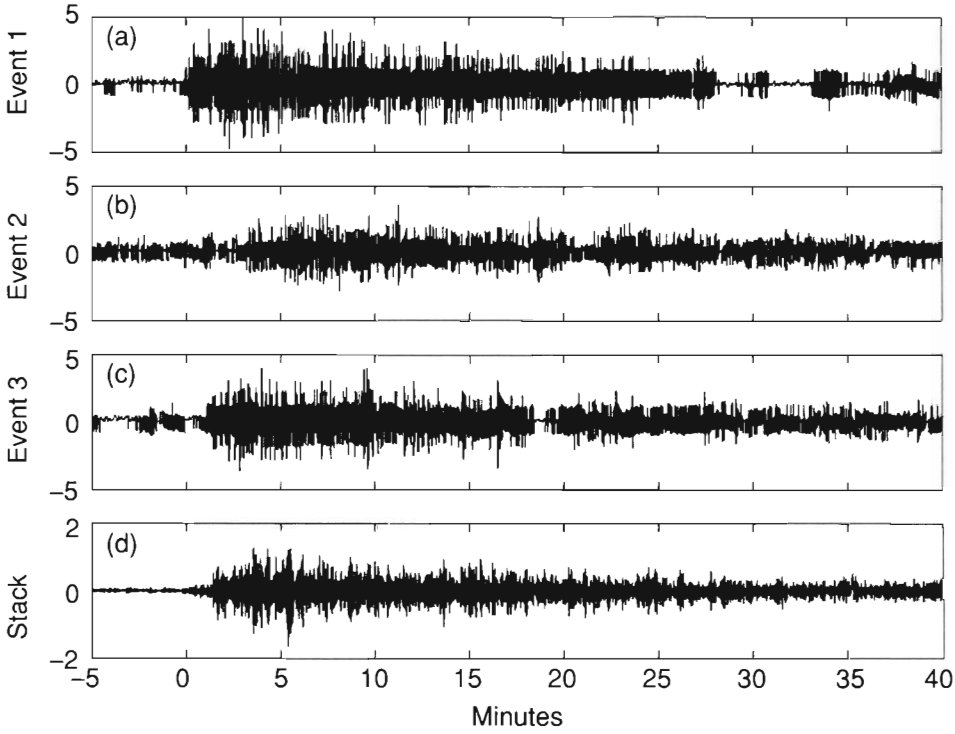

Figure 4.28. Waveform repeatability of deep moonquake source regions. Figures (a)–(c) denote typical seismograms for single events from source region A1. Waveform amplitudes are in digital units (DU). Figure (d) is a stack of waveforms meeting a given coherence criterion – the increased signal-to-noise ratio is evidenced, in particular, via the decreased noise level immediately preceding the event onset. Figure taken from (Bulow *et al.*, 2005)

deep moonquake source region is A1, as it contains the largest number (443) of individual events.

Deep source regions – also referred to in the lunar literature as deep event groups or clusters – can be located using P- and S-wave arrival times. The internal seismic velocity structure must be either assumed, or simultaneously inverted for, in moonquake location studies. As a result of the limited number of seismic stations, reliable location estimates require both P and S arrival times to be measured on all the seismic stations or on stations 15, 16 and at least one of stations 12 and 14. In practice this is usually not the case, and even where they are available, the travel time picks tend to have large uncertainties due to the noisy records. This results in trade-offs between moonquake locations and seismic velocity structure. Two approaches have been taken: in the first, sufficient travel time picks are required to be able to estimate moonquake location and seismic velocity simultaneously – the

most recent such study is that of Gagnepain-Beyneix *et al.* (2006) for which 23 deep moonquakes have sufficient arrival time picks to allow simultaneous location and velocity inversion. In the second approach, a seismic velocity model is assumed and the deep source region located using that model. This approach was adopted in the study of Nakamura (2005) in which he used a velocity model from Nakamura (1983) to locate the previously-mentioned 98 nearside clusters. The effects of different models on uncertainties in source region location are illustrated in Figure 4.5 of Bulow *et al.* (2007). Importantly, the absence of arrival picks from particular stations leads to very large uncertainties (e.g., over 20° in latitude) in deep moonquake locations.

Plate 10 shows the locations of nearside deep clusters from both the study of Nakamura (2005) and Gagnepain-Beyneix *et al.* (2006). For the Nakamura (2005) study we consider only those deep clusters for which depth estimates were determined, and for which uncertainties in the latitude and longitude of the deep cluster are less than 10°. This results in retaining 50 of his 98 nearside clusters; 20 deep source regions are common to this dataset and that of Gagnepain-Beyneix *et al.* (2006), and we distinguish these in Plate 10. The additional source regions contributed by the study of Nakamura (2005) provide improved geographical sampling compared with the Gagnepain-Beyneix *et al.* (2006) dataset alone. It is clear that the deep source regions are not distributed randomly even within some nominal region of sensitivity about the centroid of the Apollo seismic network. It has been noted (Lammlein, 1977) that the deep source regions are located in an approximately NE–SW band. Plate 10 shows qualitative agreement with this statement, but that in particular, few deep clusters are located below the nearside highlands. We discuss the geographical distribution of deep moonquake clusters further in Section 6.

4.2 Shallow moonquakes

Over the 8 years the Apollo passive seismic experiment collected data, 28 events were detected with signal characteristics that distinguish them from both meteorite impacts and deep moonquakes (Nakamura, 1977, 1980; Nakamura *et al.*, 1979). These events were originally designated as "high frequency teleseismic" (HFT) events, on the basis of the frequency content of their waveforms, and hence their stronger appearance on the short-period versus long-period instruments. Given the small number of events, the occurrence statistics of these events cannot be robustly assessed; however, unlike the deep moonquakes, there is no clear correlation with particular tidal phases (Nakamura, 1980).

Following the termination of the passive seismic experiment, there was some debate as to whether these events occur at the lunar surface, within the crust, or within the upper mantle; initially they were thought to be surface events. All 28

events occurred outside the seismic network; P- and S-wave arrival times are thus rather insensitive to the depth of the foci, and depths in the range 0 to 200 km (and even above the surface!) are permitted by the travel times alone. Nakamura *et al.* (1979) compared the observed variation in amplitude of the short period seismograms with epicentral distance with theoretical amplitude variations based on an earlier lunar seismic model (LM-761, Nakamura *et al.*, 1976). The observed amplitude variation is the most convincing evidence to date of a sub-crustal origin for the shallow moonquakes – 100 km depth was suggested (Nakamura *et al.*, 1979). This average depth is based on the amplitude–distance variation of the complete population, and was set in part by a lunar interior model, LM-761, that included a 55 km thick crust. In the light of recent revisions to estimates of the seismically determined crustal thickness (see Section 5), an average depth less than 100 km for the shallow events may be permitted.

As with the deep moonquake population, shallow moonquakes can be located either by assuming or co-estimating an internal seismic velocity model. The study of Gagnepain-Beyneix *et al.* (2006) finds eight shallow moonquakes to have sufficient travel time arrivals to allow the latter approach – inspection of Table 4.1 of their paper shows 2 of the events to have best-fit depths at the surface, 3 to have best-fit depths in the crust and 3 to have best-fit depths in the mantle, respectively. The studies of Nakamura *et al.* (1979) and Nakamura (1980) located 26 of the 28 events using the velocity model mentioned above (Plate 10). Because of the small number of shallow moonquakes we examine all 26 events, with the caveat that there may be large uncertainties in many of these locations. In general, shallow moonquakes are not located near the centers of the nearside basins, and, as has been noted previously (Nakamura *et al.*, 1979), appear to show some correlation with the edges of impact basins. The small number of events, together with uncertainties in their locations, renders statistical tests of preferred locations tenuous at best. We return to discussion of shallow moonquake locations in Section 6.

Nakamura *et al.* (1979) estimated magnitudes for all 28 shallow moonquakes by measuring the amplitude of the envelope function for the short-period seismograms. Their magnitude estimates correspond to Richter magnitudes in the range $\sim$1.5 to just under 5.0. Using displacement spectra, Binder and Oberst (1985) and Oberst (1987) estimated seismic moments and stress drops. The results indicate that most shallow quakes have stress drops of a few MPa, but that the three largest events show body wave magnitudes greater than 5.5 and stress drops of over 100 MPa.

5 Internal structure of the Moon

The mechanical properties of the outer part of the Moon determine its tectonic deformation, and these properties are intimately related to the thermal and

compositional evolution of the body. The main compositional layers in the Moon are a small core, a silicate mantle, and a less dense silicate crust. Thermally, the Moon is comprised of an outer thermal boundary layer or lithosphere across which heat is transported via conduction. Unlike larger terrestrial planetary bodies, it is unclear whether below this there is a region in which convective motions are presently occurring. The part of the lithosphere that can deform elastically is usually referred to as an effective elastic thickness, T_e (we shall refer to this simply as elastic thickness for brevity).

While we are primarily interested in lunar interior structure at depths shallower than ~1000 km, we briefly review what is understood about the deep lunar interior because it is linked to the present and past shallower structure through the Moon's thermal history. Gross geophysical constraints on lunar interior structure include the moment of inertia factor (0.3932 ± 0.0002; Konopliv *et al.*, 1998), the mean mass, and the k_2 Love number. These, together with magnetic sounding measurements (Hood *et al.*, 1999) suggest a conducting core with a radius of 340 ± 90 km. Moreover Williams *et al.* (2001) have shown that the rotation of the Moon is influenced by a dissipation source, which has been interpreted as the signature of a liquid core. Recent interior-structure models (Lognonné and Johnson, 2007) indicate that a wide range of acceptable core models in the range of 1%–2% lunar mass fit the data. Core densities less than 6000 kg/m^3 are preferred, consistent with a core containing some light element(s), in turn allowing a currently liquid state (Lognonné *et al.*, 2003; Gagnepain-Beyneix *et al.*, 2006; Khan *et al.*, 2006). To date there is no seismic constraint on lunar core size or physical state (see review in Lognonné and Johnson, 2007), though renewed attempts are being made to search for core phases in the Apollo seismic data (Bulow and Lognonné, 2007).

Several approaches can be used to probe the thermal and mechanical structure of the outer part of the Moon. Seismic data provide information on the present-day elastic properties of the lunar interior, and hence indirectly offer constraints on current compositional and thermal structure (Section 5.1). Gravity and topography data together allow investigation of models for support or compensation of topography. Typically the quantities of interest in such studies are estimates of crustal and/or elastic thickness, although models are non-unique and there are additional trade-offs with the assumed density structure. Studies of elastic thickness have mainly focused on the nearside basins that exhibit large positive gravity anomalies. The results are rather inconclusive and, as alternative constraints are provided by the locations of tectonic features, we discuss elastic thickness in the context of integrated tectonic studies of the nearside basins (Section 6). Here we focus on the constraints on global crustal structure provided by gravity and topography data (Section 5.2) and compare these results with those provided by the seismic data.

5.1 Seismological constraints

From a practical perspective, the limited source–receiver geometries and the noisy seismograms mean that only averaged 1-D seismic velocity profiles can be established. Inspection of Plate 10 shows that these velocity–depth profiles will mainly reflect seismic velocities beneath the lunar maria. Of particular interest are discontinuities or sharp velocity gradients corresponding to major compositional boundaries.

By analogy with Earth, the lunar seismological crust–mantle interface is defined by a velocity discontinuity or steep gradient ($>0.1\ \mathrm{km\,s^{-1}\,km^{-1}}$), below which the P-wave velocity should attain a value of at least $7.6\ \mathrm{km\,s^{-1}}$ (Plate 11). Velocity structure at crustal depths is mainly constrained by P- and S-wave arrival times due to impacts (see discussion in Lognonné and Johnson, 2007) and variations among existing models reflect the limited seismic ray path coverage at depths less than 60 km. In terrestrial studies, crustal thickness can be obtained by studies of converted seismic phases; however, the latter are not readily observed on lunar seismograms and only phases from the Apollo 12 station have been successfully investigated (Vinnik *et al.*, 2001; Gagnepain-Beyneix *et al.*, 2006).

While there are uncertainties in crustal thickness estimates, three main conclusions can be drawn from the seismological data. First, the averaged crustal thickness reflects primarily crustal structure at the Apollo 12 and 14 sites. Second, recent investigations indicate that a 30 to 45-km thick crust at the Apollo 12/14 sites (Khan and Mosegaard, 2002; Lognonné *et al.*, 2003; Gagnepain-Beyneix *et al.*, 2006) is preferred over previous estimates of 58 km (Nakamura, 1983; and see earlier work by Toksöz, 1974). Third, these more recent 1-D crustal thickness estimates, and a recent attempt to map geographical variations in crustal thickness using the Apollo seismic data (Chenet *et al.*, 2006), are consistent with those based on analyses of gravity and topography data (see Wieczorek *et al.*, 2006 and Section 5.2).

It is not possible to resolve whether the correct model for the seismological crustal structure is one of distinct constant-velocity layers, or gradually increasing velocity with depth. Perhaps the most succinct summary of the seismic data is that it is broadly consistent with a crustal structure in which there are two major compositional layers – an upper, very feldspathic, and lower, moderately feldspathic, crust – consistent with inferences from gravity and topography data (Wieczorek *et al.*, 2006). Seismologically, higher velocities are associated with the noritic lower crust. Some suggestions of a mid-crustal reflector have been made (e.g., the 20 km discontinuity of Khan and Mosegaard, 2002), but this is not observed in all models. Furthermore, a near-surface regolith and fractured layer results in scattering of seismic energy and significantly reduced seismic velocities in the upper $\sim$1 km (see review in Wieczorek *et al.*, 2006).

P- and S-wave arrival times from moonquakes provide some information on seismic velocity structure down to ~1000 km depth – i.e., the depth of the deep moonquake source regions. A review of mantle seismic velocity structure is beyond the scope of this chapter and can be found in Lognonné and Johnson (2007). In general, P-wave velocities in the lunar mantle are around 8 km s^{-1} and S-wave velocities are around 4.5 km s^{-1}. Of interest here are the predictions of thermal models based on these seismic velocity profiles for temperatures in the deep moonquake source regions and we return to this in Section 6.2.

5.2 Constraints from gravity and topography

Global measurements of gravity and topography data allow constraints to be placed on crustal and lithospheric structure. A thorough review of this topic can be found in Wieczorek *et al.* (2006) and we summarize only the main points here. Lunar topography data sets were reviewed in Section 2. For analyses involving both gravity and topography data, the spherical harmonic topography model derived from the Clementine data (GLTM2c, Smith *et al.*, 1997) is the most useful, and contains information to spherical harmonic degree and order 90, equivalent to a maximum spatial resolution of ~120 km. Gravity field measurements were obtained during the Lunar Prospector mission; the most recent gravity field model is that of Konopliv *et al.* (2001) which contains information to spherical harmonic degree and order 150, equivalent to a maximum spatial resolution of 72 km (Plates 12A,B).

Nearside free-air gravity anomalies (Plate 12A) are typically close to zero over the highland regions, indicating isostatic compensation of topography. Large positive gravity anomalies are seen over several nearside basins, in particular Imbrium, Serenitatis, Crisium, Nectaris and Humorum. These "mascons" were first observed in Lunar Orbiter tracking data (Muller and Sjogren, 1968), and have been mapped in more detail by Lunar Prospector. Peak anomalies are over 300 m Cal. The farside gravity field is poorly determined because of the lack of tracking data away from the limbs on the farside.

Three different approaches can be used to estimate lunar crustal thickness from gravity and topography; one of these techniques also allows estimation of elastic thickness. For topography compensated solely by variations in crustal thickness (commonly referred to as Airy compensation), the ratio of geoid height to topography over a region is proportional to the average crustal thickness. This approach was pioneered by Ockendon and Turcotte (1977) in cartesian coordinates (i.e., the region of interest must be small enough for planetary curvature to be negligible) and adapted for use in spherical coordinates by Wieczorek and Phillips (1998). Regions where Airy isostasy clearly does not hold (e.g., mascons) can easily be excluded

from analyses. Using this approach Wieczorek *et al.* (2006) infer a globally averaged crustal thickness of 49 ± 15 km. Crustal thicknesses at Apollo sites 12 and 14 are in the range 16–56 km, depending on the crustal and mantle densities assumed, and are consistent with the more recent seismologically-based inferences of crustal thickness (Khan and Mosegaard, 2002; Lognonné *et al.*, 2003; Gagnepain-Beyneix *et al.*, 2006).

Spectral admittance techniques examine the relationship between gravity and topography in the wavenumber domain. The advantage over the geoid–topography ratio approach is that if topography is supported by more than one mechanism (e.g., a combination of crustal thickening and lithospheric flexure), then it may be possible to identify these different contributions by their spectral signature, and furthermore to estimate both crustal and elastic thickness for a given region. The drawback is that it is less easy to investigate localized regions using spectral approaches, although work by Wieczorek and Simons (2005) make this problem more tractable (for a full discussion, see Wieczorek *et al.*, 2006, and references therein). Localized spectral admittance modeling suggests mean crustal thicknesses beneath the lunar basins in the range 35–70 km (Aoshima and Namiki, 2001), and the two basins that likely satisfy a pre-mare isostatic assumption (the density deficit due to excavation of the basin was balanced by an associated positive density contrast at depth due to uplift of the crust–mantle boundary) (Wieczorek and Phillips, 1998) both yield a mean crustal thickness of 50 km.

Global crustal thickness models have also been constructed using lunar gravity and topography data (Neumann *et al.*, 1996; Wieczorek and Phillips, 1998; Wieczorek *et al.*, 2006). The contribution to the gravity field due to the surface topography is subtracted from the free-air gravity and the resulting gravity anomaly (the Bouguer anomaly) inverted for relief on the crust–mantle boundary. Previous studies have investigated both single- and dual-layer crustal structure: all models show substantial crustal thinning beneath major basins, and several of the mascon basins exhibit super-isostatic thinning (i.e., uplift of the crust–mantle boundary to a depth shallower than that needed for hydrostatic equilibrium beneath an excavated basin). In two-layer crustal models, the upper crust is completely removed at major basins, and the observed gravity anomalies can only be matched by including further thinning of the lower crust and the contribution of a mare basaltic load (see Wieczorek *et al.*, 2006).

6. Basin-localized tectonics and seismicity

The temporal and spatial patterns of deformation in the nearside maria, characterized by basin-concentric and basin-radial wrinkle ridges and arcuate and linear rilles, provide important, albeit incomplete, information on the tectonic history of

the lunar basins. The large positive gravity anomalies over several of the nearside basins indicate uncompensated positive density anomalies that likely result from a combination of loading by mare basalts, intrusion, and a possible super-isostatic pre-mare basin state (see Section 5). The mare basins exhibit low elevations and generally flat topography (see Section 2 and Plates 6A,B); in the case of Mare Serenitatis, a long-wavelength, low-amplitude rise is observed, with the highest topography in the center of the basin. Taken together, these observations have been used to both probe the sub-mare mechanical structure of the lunar lithosphere, and to develop loading models that can explain the observed tectonism.

6.1 Lithospheric structure beneath mare basins

The classic loading model of a mass concentration due to the mare basalts on an impact-thinned and impact-weakened lithosphere results in compression in the interior of the basin and extension near the margins (Phillips *et al.*, 1972; Melosh, 1978; Solomon and Head, 1979, 1980; Freed *et al.*, 2001). Early mascon tectonic models involved axisymmetric loading of a thin elastic plate and these predict basin-interior compression (see Section 6.2) and concentric normal faulting near the basin margins. For a given basin, the radial distance to the concentric rilles and to the wrinkle ridges can be used to estimate elastic lithospheric thickness, T_e, at the time of loading. This approach was adopted in a series of studies (Comer *et al.*, 1979; Solomon and Head, 1979, 1980), and combined with age information for the two classes of tectonic features to investigate spatial and temporal variations in T_e. Solomon and Head (1980) examined eight basins: Imbrium, Serenitatis, Crisium, Humorum, Grimaldi, Orientale, Smythii, and Nectaris, and concluded that T_e at the time of rille formation (i.e., ages >3.6 Ga) was generally less than about 75 km, but showed considerable variations among the different basins, ranging from less than 25 km at Grimaldi basin to up to 75 km at Imbrium and Crisium. T_e estimates at the time of graben formation (i.e., younger ages) are greater and generally at least 100 km, implying cooling and thickening of the lithosphere over time. In addition, T_e at the time of wrinkle-ridge formation shows less between-basin variability (Solomon and Head, 1980).

As mentioned briefly in Section 5, gravity and topography data can be used to estimate T_e. Estimates derived in this way will not necessarily correspond to T_e at the time of loading, since the present-day gravity signature of the mare basins is being matched. Such an approach has been attempted for the lunar basins, though with limited success. Arkani-Hamed (1998) found T_e in the range 30 to 50 km beneath six nearside basins including Serenitatis, and T_e of 20 km beneath Orientale; however, Aoshima and Namiki (2001) concluded that for Orientale and Serenitatis, T_e is not well constrained. A study by Crosby and McKenzie (2005)

indicates that T_e at Imbrium must be greater than 25 km. It is not surprising that gravity and topography studies have returned a variety of estimates for T_e, since such studies require a-priori assumptions about the vertical density structure, and this is not straightforward to establish given the likely complex loading history of the mare basins.

6.2 Predictions for tectonic deformation

The mascon loading model described above predicts stresses that would result in the following pattern of faulting with increasing radial distance from the basin center: basin-interior radial thrust faults (the maximum principal stress σ_1 is horizontal, minimum principal stress σ_3 = vertical stress σ_v), a zone of strike-slip faulting (σ_1 is horizontal, $\sigma_2 = \sigma_v$), and finally concentric normal faulting near the basin margins (σ_1 is vertical, $\sigma_1 = \sigma_v$) (Melosh, 1978; Freed *et al.*, 2001). Two issues are immediately apparent: the absence of documented strike-slip faults in mare basins, and the dominance of concentric rather than radial thrust faults.

The zone of strike-slip faults in mare mascons is predicted by Anderson's criterion (Anderson, 1951). It results from the transition of σ_v from the minimum to the maximum principal stress (see Schultz *et al.*, Chapter 10). The absence of evidence of strike-slip faulting in the mare mascons has been described as the "strike-slip faulting paradox" (Freed *et al.*, 2001; Wieczorek *et al.*, 2006). A number of factors may act to suppress the formation of lunar strike-slip faults. These include the preexisting state of stress in the lunar lithosphere (Solomon and Head, 1980), the depth of fault nucleation (Golombek, 1985), and the load history and evolution of stress (Schultz and Zuber, 1994). Freed *et al.* (2001) showed that the predictions of a large strike-slip zone and the dominance of radial thrust faults are the result of the use of elastic plate models and the Anderson faulting criterion. They employed a viscoelastic model and showed that the inclusion of lunar curvature and the use of the fault criterion of Simpson (1997) (that accounts for stress transitions), significantly reduce the zone of predicted strike-slip faulting and permit a wider range of faulting styles than the classic mascon model. In addition, strike-slip faulting is further inhibited by larger radii loads, loading of a thin lithosphere (e.g., in the Freed *et al.* (2001) study, a 25 km versus 100 km lithosphere is considered), an initially super-isostatic stress state, and the inclusion of heterogeneities in crustal strength.

Another paradox in the mascon tectonic model arises from the discrepancy between the predicted and observed pattern of wrinkle ridges in the maria (see Wieczorek *et al.*, 2006). As mentioned above, the mascon model predicts basin-interior, radial oriented thrust faulting. The dominant pattern of wrinkle ridges in the interiors of many of the mascons, however, is concentric (see Plate 6A).

Many of the radial oriented wrinkle ridges occur near the basin margins, closer to the location of concentric graben. In Mare Serenitatis, basin-radial oriented wrinkle ridges are crosscut by prominent arcuate graben of Fossae Plinius (see Figure 4.3). Freed *et al.* (2001) concluded that both concentric and radial mare ridges are expected if a global compressive stress bias and the loading history from the mare basalts are accounted for. Two other factors explored by Freed *et al.* (2001) may also influence the pattern of wrinkle ridges. One is the geometry of the load and the other is the pre-mare compensation state of the basin (see Wieczorek *et al.*, 2006). A radial pattern of mare ridges is predicted if the basin was initially sub-isostatic, and rebound occurred after emplacement of the mare basalts (Freed *et al.*, 2001, Fig. 12). A concentric pattern of mare ridges is favored if the basin was initially super-isostatic, and subsidence occurred after the emplacement of the mare basalts.

The geometry of the load from the mare basalts also has a strong influence on the expected pattern of mare ridges (Freed *et al.*, 2001, Fig. 10). A radial pattern of mare ridges is predicted if the mare basalts are thicker in the center of the basin than near its margin. A concentric pattern of ridges is expected if the mare basalts are more uniform in thickness. It is generally concluded that the mare basalts have the greatest thickness in the centers of the basins, based on a decrease in the number of pre-mare craters and ALSE subsurface profiles (see Baldwin, 1970; Wilhelms, 1987). Insight into the geometry of the load from the mare basalts may be obtained from an analysis of the long-wavelength topography of the basins. As discussed in Section 2.1.1, Clementine LIDAR data over Mare Serenitatis show a topographic high in the mare surface located in the interior of the basin. In contrast, Mare Crisium and Mare Humorum have generally flat interior floors. Mare Imbrium also has a flat floor, but it has a pronounced regional slope. The mare surface at the north rim of Imbrium may be as much as 1000 m higher than at the south rim. Unlike Mare Serenitatis, there is no obvious spatial correlation between interior rings of wrinkle ridges and elevation changes in the Mare Imbrium, Mare Crisium, or Mare Humorum.

As discussed in Section 5, gravity data collected by the Lunar Orbiters, the Apollo missions, Clementine, and the Lunar Prospector mission, indicate that Mare Imbrium, Mare Serenitatis, Mare Crisium, Mare Humorum, and Mare Nectaris have strong positive gravity anomalies ringed by negative anomalies (Zuber *et al.*, 1994, Fig. 2b; Lemoine *et al.*, 1997, Plate 1; Konopliv *et al.*, 1998, Fig. 1a). Positive anomalies are attributed to the uncompensated mare basalts (Phillips *et al.*, 1972) and the presence of a dense mantle "plug" formed by post-impact mantle rebound (Wise and Yates, 1970; Solomon and Head, 1979). The surrounding negative anomaly suggests subsurface mass deficiencies that result from crustal thickening related to basin formation or modification (Lemoine *et al.*, 1997). Future high-resolution gravity data, e.g., from the Gravity Recovery and Anterior

Laboratory or GRAIL mission, are needed to evaluate possible contributions to the negative anomalies from ringing due to the finite spherical harmonic expansion.

Pre-Lunar Prospector mission gravity models often show lunar mascons with "bull's eye" patterns, with the high located roughly in the center of the mare (e.g., Lemoine *et al.*, 1997, GLGM-2 free-air model). This pattern would suggest an axially symmetric, Gaussian-shaped accumulation, with the greatest thickness of the basalts near the basin center if the dominant contribution to the gravity anomaly is from the basalt fill (Phillips *et al.*, 1972). The most recent lunar gravity models that incorporate Lunar Prospector data (Konopliv *et al.*, 1998, 2001; Konopliv and Yuan, 1999), however, show that anomalies for the mare mascons have broad plateaus throughout the mare interior. The spatial correlation between the edges of the positive anomalies and basin-interior wrinkle-ridge rings in Mare Imbrium, Mare Serenitatis, Mare Crisium, and Mare Humorum is striking (Plate 12A). This supports the interpretation that positive anomalies are dominated by the near-surface mare fill (Phillips *et al.*, 1972; Konopliv *et al.*, 1998, 2001; Watters and Konopliv, 2001), since contributions to the gravity anomalies from topography on the crust–mantle boundary will be more smoothly varying. This suggests that the basalt sequence in the interior of the basin may be generally uniform in thickness and thin rapidly at the margins. The modeling of Freed *et al.* (2001) suggests that a more uniform thickness of mare basalts will result in a basin-interior concentric pattern of mare ridges with radial mare ridges near the margin, consistent with the observed distribution. Interestingly, Mare Nubium has no associated mascon, but is dominated by radial wrinkle ridges. Similarly there is a group of radially oriented wrinkle ridges at the western edge of Mare Tranquillitatis, with no associated free-air gravity anomaly. Finally, the fact that some concentric graben crosscut radial oriented mare ridges, as is the case in Mare Serenitatis, suggests some mare have a more complex stress history, where zones dominated by compression and extension have changed over time.

Not all the Moon's wrinkle ridges and graben are associated with mascons. The most significant occurrence of nearside tectonic features outside a lunar mascon is in Oceanus Procellarum (see Plates 6A and 12A). Although the youngest mare basalt units, estimated to be ~1.2 Ga old (Plate 9A) (Hiesinger *et al.*, 2003), occur in Oceanus Procellarum, it lacks a strong positive anomaly and the spatial correlation of the anomaly with the wrinkle ridges indicative of mascons. Also, many graben are radial to Procellarum (Plate 6A). Only hints of weak to moderate positive and negative anomalies are resolved in the current gravity model (Plate 12A). The origin of Procellarum remains uncertain. The hypothesis that Oceanus Procellarum is a giant impact basin (see Wilhelms, 1987) is still debated (see Hiesinger and Head, 2006). Current geophysical evidence suggests overprinting by known basins, but provides no definite indication of a giant pre-Nectarian

basin (Neumann *et al.*, 1996). An alternative hypothesis is that Procellarum is connected to the Imbrium event, possibly the outermost ring structure of Imbrium (Spudis *et al.*, 1988b; Spudis, 1993) having formed by down-dropping on bounding normal faults (Cooper *et al.*, 1994).

6.3 Basin-localized seismicity

The deep moonquake source regions generally occur around the edges of, or beneath, the major nearside basins (Plate 10). Furthermore, with the exception of two source regions in Serenitatis and one in Crisium, deep moonquakes generally occur exterior to the concentric wrinkle ridges and hence exterior to large positive gravity anomalies. Deep moonquake depths are of course too deep to indicate any direct correlation between their geographical distribution and the distribution of surface tectonic features. However, their spatial distribution suggests that the influence of long-lived deep lateral thermal and/or compositional heterogeneities is associated with either basin formation and/or mare basalt production.

Very little is known about deep moonquake source regions. A routine procedure in analyzing earthquake data is the investigation of focal mechanisms; however, this has not been possible for deep moonquakes because of the limited number of receivers and the paucity of deep moonquakes that occurred inside the seismic array. Some attempts have been made to extract information about putative fault plane orientations by examining whether elastic tidal stresses resolved onto a given plane can be used to predict moonquake occurrence times. However, such studies have not reached consistent conclusions because of differing assumptions regarding the role of shear versus normal stresses, a-priori background stress fields (e.g., due to global thermal contraction), and the lack of removal of the long-term tidal stress (Lammlein, 1977; Toksöz *et al.*, 1977; Cheng and Toksöz, 1978; Minshull and Goulty, 1988). In addition, most previous work that has investigated the relationship between tidal stress and moonquake occurrence has focused on the A1 source region because of the large number of A1 events. Comparison of results among existing studies is further hampered by differences in the choice of coordinates systems used (Cheng and Toksöz, 1978; Minshull and Goulty, 1988). A recent study (Weber *et al.*, 2009) has examined clusters with more than 30 events (51 in total), and investigated plane orientations that minimize the variance in stresses at moonquake occurrence times for a Coulomb failure criterion (i.e., failure can result from a combination of normal and shear stresses). Moonquake occurrence times at some of the clusters examined appear to be quite well predicted by failure on a plane, however, at other clusters no particular plane orientation appears to be preferred. Importantly, nearby clusters do not seem to respond similarly to tidal

forcing, suggesting that the brittle failure is controlled by physical properties that vary on spatial scales much shorter than inter-cluster distances.

This latter inference is supported by earlier and recent investigations of the possible spatial extent of deep moonquake source regions. Investigations of the A1 source region suggest that the hypocenters of individual events are confined within a radius of about 1 km (Nakamura, 1977, 2007), and 12 other clusters appear to have a similarly small spatial extent (Nakamura, 2007).

An unresolved, and major, issue is why brittle failure occurs at depths of 700 to 1000 km. Recent thermal models based on seismic data suggest temperatures of 1100 to 1400 °C (Lognonné *et al.*, 2003), and although those based on electromagnetic data are lower (Khan *et al.*, 2007), all estimates suggest a regime in which ductile, rather than brittle, failure should occur.

As with the deep moonquakes, many outstanding questions surround the cause and locations of shallow moonquakes. As mentioned earlier, shallow moonquakes have been suggested to occur at the edges of basins (see Plate 10), plausibly related to lateral heterogeneities in mechanical structure. If these events are in fact upper mantle events, as suggested by Nakamura *et al.* (1979), then any connection to surface tectonic features is unlikely. If however, some of these events do occur within the crust, then any association with tectonic features would be of interest.

As reviewed earlier, the majority of basin-localized tectonism mainly ceased ~1.2 Ga, and the youngest class of tectonic features, lobate scarps, are not basin-localized. However, current seismicity does appear to be largely basin-localized, offering the tantalizing suggestion that lateral heterogeneities in temperature, and/or composition, and/or mechanical structure resulting from basin and mare-basalt formation have persisted to the present day.

7 Global strain from young lobate scarps

The relatively small-scale lobate scarps may be the youngest tectonic features on the Moon. The source of compressional stresses that formed the young lobate scarps may have been thermal stresses from interior cooling. Thermal models for a magma ocean (Solomon and Chaiken, 1976; Solomon and Head, 1979) and an initially total molten Moon (Binder and Lange, 1980) both predict a late-stage compressional stress bias in the lunar lithosphere. The true distribution of thrust faults in the lunar highlands cannot be evaluated at present because most of the scarps can only be identified in Apollo Panoramic camera images of the lunar equatorial zone, and in some high-resolution Lunar Orbiter III and V images. Of the ~20% of the lunar surface imaged by the Apollo Panoramic Cameras, only about 10% was imaged with the optimal lighting geometry for detecting the lobate scarps. This makes an accurate estimate of the strain expressed by the lobate scarps difficult. However,

the contractional strain in the area covered by high-resolution Panoramic Camera images can be estimated using the D–L relationship of the lobate scarp thrust faults (see Section 2.5). If the D–L relationship of a fault population is known, the strain can be calculated using fault lengths alone (Scholz and Cowie, 1990; Cowie *et al.*, 1993). The strain for faults where the fault length $L \geq$ the maximum depth of faulting is given by

$$\varepsilon = \frac{\cos(\theta)}{A} \sum_{k=1}^{n} D_k L_k, \tag{4.2}$$

where θ is the fault plane dip, A is the survey area, n is the total number of faults, and $D = \gamma L$ (Cowie *et al.*, 1993). Using the value of γ of $\sim 1.2 \times 10^{-2}$ for $\theta = 30°$ (see Section 2.5) and the total length of the lobate scarps measured in this study, the strain is estimated to be ~0.008% for a study area covering about 10% of the lunar surface. For comparison, the strain reflected by the lobate scarps on Mercury is ~0.06% (for $\theta = 30°$) (Watters and Nimmo, Chapter 2; Watters *et al.*, 2009). Thus, the contractional strain from the young lobate scarps on the Moon appears to be nearly an order of magnitude less than the strain from the larger scale thrust faults on Mercury.

If the lobate scarps are the result of thermal stresses from global cooling, then the surface strain can be used to estimate the corresponding radius change of the Moon. The pre-deformation lunar radius R_u is related to the contractional strain by

$$R_u = \left[\frac{R_d^2}{\varepsilon + 1} \right]^{0.5}, \tag{4.3}$$

where the radius change is expressed by $\Delta R = R_d - R_u$ where R_d is the post-deformation (current) radius (Watters and Nimmo, Chapter 2). Assuming the ~10% of the lunar surface covered by Panoramic Camera images is representative of the entire surface, a strain ε of ~0.008% corresponds to a ΔR of ~70 m. The isotropic stresses σ resulting from global contraction (Melosh and McKinnon, 1988) are given by

$$\sigma = 2\mu \frac{(1+\nu)}{(1-\nu)} \frac{\Delta R}{R_d}, \tag{4.4}$$

where μ is the shear modulus, and ν is the Poisson's ratio. The stress corresponding to the relatively small estimated radius change is <10 MPa.

Global contraction is predicted on the basis of thermal evolution models, but distributed large-scale lobate scarp thrust faults like those on Mercury are not found on the Moon. In an effort to reconcile this mismatch, Pritchard and Stevenson (2000) concluded that the near-surface regolith might be able to accommodate

more contractional strain than intact rock before failing, or the Moon may have experienced a non-monotonic thermal evolution, or that contractional strain was accommodation by numerous small faults (Weisberg and Hager, 1998). Thus, relating surface strain to internal processes may not be straightforward and the lack of large-scale thrust faults may not strongly constrain the change in lunar volume (see Shearer *et al.*, 2006). However, the small-scale lobate scarp thrust faults, possibly rooted in the regolith (or megaregolith), may be an expression of late-stage global contraction. If this is the case, they could provide important insight into the recent compressional stress state of the lunar lithosphere.

Thermal history models based on the formation of a magma ocean (Solomon and Chaiken, 1976; Solomon and Head, 1979) and an initially totally molten Moon (Binder and Lange, 1980) both predict a late-stage compressional stress bias in the lunar lithosphere. The initially totally molten model predicts stresses of up to 350 MPa (Binder and Lange, 1980; Binder and Gunga, 1985). Such a high state of global compressional stress might be expected to result in thrust faults comparable to large-scale lobate scarp thrust faults on Mercury and Mars. The magnitude of compressional stresses predicted by the magma ocean thermal history model is less than 100 MPa after the end of the period of heavy bombardment (Solomon and Chaiken, 1976; Solomon and Head, 1979). Although the estimated strain from the lunar lobate scarps must be considered a lower limit in light of the possibility that significant contractional strain may go without expression (Pritchard and Stevenson, 2000), they support thermal history models predicting a small change in lunar radius of about ± 1 km in the last 3.8 Ga (Solomon and Chaiken, 1976; Solomon and Head, 1979, 1980).

8 Conclusions and outstanding questions

The majority of the Moon's large-scale tectonic landforms occur on the nearside, in and around the maria. This basin-localized tectonics is reflected in the wrinkle ridges and linear and arcuate rilles or troughs. Wrinkle ridges are the expression of crustal shortening in the basin interiors, while linear and arcuate rilles express crustal extension at basin margins and in the adjacent highlands. The spatial distribution of contractional and extensional tectonic features is the result of lithospheric flexture due to mascon loading. Basin-localized crustal extension ceased $\sim$3.6 Ga while crustal shortening continued to as recently as $\sim$1.2 Ga. Crustal extension may have ceased when compressional stresses from global contraction were superimposed on flexural extensional stress due to mascon loading.

Mascon gravity anomalies exhibit broad plateaus throughout mare interiors. In some basins, interior wrinkle-ridge rings correlate spatially with the edges of the positive anomalies, suggesting that the mare basalt fill results in a disk-like load.

Stress models of lunar mascons suggest that the spatial distribution of the wrinkle ridges and rilles are best fit by a uniform thickness of mare basalts.

Exterior to the nearside maria, lobate scarps are the dominant lunar tectonic feature. These small-scale thrust faults are less than 1 Ga and are likely among the youngest endogenic features on the Moon. Young lobate scarp thrust faults support late-stage compression of the lunar crust. The lobate scarps express a relatively small contractional strain (~0.008%), corresponding to a radius change of ~70 m. This is consistent with thermal history models that predict a small change in lunar radius in the last 3.8 Ga.

The Apollo seismic data provide information on the crustal and upper mantle velocity structure of the Moon, from which interior thermal profiles have been constructed. Naturally occurring lunar seismicity comprises two distinct classes of events: (1) a few (28) shallow moonquakes that occur at depths of 100 km or less and can result in stress drops of over 100 MPa, and (2) thousands of small stress drop moonquakes that originate from distinct source regions at 700 to 1000 km depth; a given source region exhibits moonquakes with tidal periods and repeatable waveforms. The deep moonquake source regions cluster around the edges of nearside basins or beneath them. Limited information regarding these source regions is available – the failure volumes appear to be small (on the order of 1 km^3), and it is unclear whether the canonical view of failure on a plane describes these quakes. The spatial distribution of deep moonquakes suggests that they may be related to long-lived, deep, lateral thermal and/or compositional heterogeneities associated with either basin formation and/or mare basalt production. Shallow moonquakes are mostly distributed around the edges of major basins. The spatial distribution of some moonquakes and their approximate correlation with tectonic features suggests that there may be current tectonic activity on the Moon.

Many outstanding questions remain to be addressed using data returned by recent lunar missions like KAGUYA (SELENE), Chang'e-1 and Chandrayaan-1 and the current Lunar Reconnaissance Orbiter mission. Critical to understanding the tectonic history of the Moon is determining the global distribution and ages of the lobate scarp thrust faults. This will require global high-resolution imaging (2 m/pixel or better). Elucidating the origin of tectonic stresses in nearside maria without associated mascons is also important in more fully understanding lunar tectonism. Related to this question is determining the origin of Oceanus Procellarum. The non-uniqueness inherent to the problem of interpreting gravity anomalies over the lunar basins could be significantly helped by better constraints on the depths of mare basalts. The radar sounder on KAGUYA has already extended our knowledge of subsurface interfaces beneath the maria gained from the ALSE experiment. Additional knowledge regarding the depths of mare basaltic fill is clearly an important constraint in tectonic loading models.

Continuous, broad-band, seismic measurements made over a period of at least 6 years by a surface geophysical network, such as the proposed International Lunar Network (ILN) are essential to further our understanding of the lunar interior. Source mechanisms for both deep and shallow moonquakes are needed, and the underlying cause of deep moonquakes is one of the outstanding problems in lunar geophysics. Essential to understanding connections between current seismicity and current or past tectonism are accurate moonquake locations for both deep and shallow events. These, in turn, are needed for improved determination of interior structure. Clearly a major gap in our understanding of lunar tectonism results from the very limited knowledge of crustal structure. For example, more detailed crustal imaging will aid in understanding the depth extent and origin of faulting.

The prospect of returning humans to the Moon has the potential to continue and expand on the wealth of lunar science made possible by the Apollo missions. Our ability to unravel the mysteries of the Moon's origin and geologic evolution may ultimately depend on a program of investigation that combines robotic missions with human exploration.

Acknowledgments

We wish to thank Paul Spudis and Walter Kiefer for their thorough and thoughtful reviews that greatly improved the chapter. This work was supported by the National Aeronautics and Space Administration under Grants issued through the Office of the Planetary Geology and Geophysics Program.

References

Anderson, E. M. (1951). *The Dynamics of Faulting and Dyke Formation, with Applications to Britain*. Edinburgh, UK: Oliver & Boyd.

Aoshima, C. and Namiki, N. (2001). Structures beneath lunar basins: Estimates of Moho and elastic thickness from local analysis of gravity and topography (abs.). *Lunar Planet. Sci. Conf. XXXII*, 1561–1562. Houston, TX: Lunar and Planetary Institute (CD-ROM).

Archinal, B. A., Rosiek, M. R., Kirk, R. L., and Redding, B. L. (2006). The Unified Lunar Control Network 2005, USGS Open File Report 2006–1367. http://pubs.usgs.gov/of/2006/1367/.

Arkani-Hamed, J. (1998). The lunar mascons revisited. *J. Geophys. Res.*, **103**, 3709–3739.

Baldwin, R. B. (1963). *The Measure of the Moon*. Chicago, IL: University of Chicago Press.

Baldwin, R. B. (1965). *A Fundamental Survey of the Moon*. New York, NY: McGraw-Hill.

Baldwin, R. B. (1970). A new method of determining the depth of the lava in lunar maria. *Astron. Soc. Pacific Publ.* **82**, 857–864.

Binder, A. B. (1982). Post-Imbrian global lunar tectonism: Evidence for an initially totally molten Moon. *Earth, Moon, and Planets*, **26**, 117–133.

Binder, A. B. and Gunga, H.-C. (1985). Young thrust-fault scarps in the highlands: Evidence for an initially totally molten Moon. *Icarus*, **63**, 421–441.

Binder, A. B. and Lange, M. A. (1980). On the thermal history, thermal state, and related tectonism of a Moon of fission origin. *The Moon*, **17**, 29–45.

Binder, A. B. and Oberst, J. (1985). High stress shallow moonquakes: Evidence for an initially totally molten Moon. *Earth Planet. Sci. Lett.*, **74**, 149–154.

Boyce, J. M. (1976). Ages of flow units in the lunar nearside maria based on Lunar Orbiter IV photographs. *Proc. Lunar Planet. Sci. Conf. 7*, 2717–2728.

Brennan, W. J. (1975). Modification of premare impact craters by volcanism and tectonism. *The Moon*, **12**, 449–461.

Brennan, W. J. (1976). Multiple ring structures and the problem of correlation between lunar basins. *Proc. Lunar. Planet. Sci. Conf. 7*, 2833–2843.

Bryan, W. B. (1973). Wrinkle-ridges as deformed surface crust on ponded mare lava. *Geochim. Cosmochim. Acta*, **1**, (Suppl.), 93–106.

Bulow, R. and Lognonné, P. (2007). Lunar internal structure from reflected and converted core phases (abs.). *Eos Trans. AGU*, P51B-0483.

Bulow, R., Johnson, C. L., and Shearer, P. (2005). New events discovered in the lunar apollo seismic data. *J. Geophys. Res.*, **110**, E10003, doi:10.1029/2005JE002414.

Bulow, R., Johnson, C. L., Bills, B., and Shearer, P. (2007). Temporal and spatial properties of some deep moonquake clusters. *J. Geophys. Res.*, **112**, E09003, doi:10.1029/2006JE002847.

Carr, M. H. (1969). Geologic map of the Alphonsus region of the Moon. U.S. Geol. Surv. Map 1–599 (RLC-14), scale 1:250 000.

Cartwright, J. A., Trudgill, B. D., and Mansfield, C. S. (1995). Fault growth by segment linkage: An explanation for scatter in maximum displacement and trace length data from the Canyonlands grabens of SE Utah. *J. Struct. Geol.*, **17**, 1319–1326.

Cartwright, J. A., Mansfield, C. S., and Trudgill, B. D. (1996). The growth of normal faults by segment linkage. *Geol. Soc. Am. Spec. Publ.*, **99**, 163–177.

Chenet, H., Lognonné, P., Wieczorek, M., and Mizutani, H. (2006). Lateral variations of lunar crustal thickness from Apollo seismic dataset. *Earth Planet. Sci. Lett.*, **243**, 1–14.

Cheng, C. H. and Toksöz, M. N. (1978). Tidal stresses in the Moon. *J. Geophys. Res.*, **83**, 845–853.

Clark, R. and Cox, S. (1996). A modern regression approach to determining fault displacement–length scaling relationships. *J. Struct. Geol.*, **18**, 147–154.

Colton, G. W., Howard, K. A., and Moore, H. J. (1972). Mare ridges and arches in southern Oceanus Procellarum, Photogeology. *Apollo 16 Prel. Sci. Rep., NASA Spec. Publ.*, **SP-315**, 29–90 – 29–93.

Comer, R. P., Solomon, S. C., and Head, J. W. (1979). Elastic lithospheric thickness on the Moon from mare tectonic features: a formal inversion. *Proc. Lunar Planet. Sci. Conf. 10*, 2441–2463.

Cook, A. C., Watters, T. R., Robinson, M. S., Spudis, P. D., and Bussey, D. B. J. (2000). Lunar polar topography derived from Clementine stereoimages. *J. Geophys. Res.*, **105**, 12 023–12 033.

Cooper, B. L., Carter, J. L., and Sapp, C. A. (1994). New evidence for graben origin of Oceanus Procellarum from lunar sounder optical imagery. *J. Geophys. Res.*, **99**, 3799–3812.

Cowie, P. A. and Scholz, C. H. (1992a). Physical explanation for the displacement–length relationship of faults using a post-yield fracture-mechanics model. *J. Struct. Geol.*, **14**, 1133–1148.

Cowie, P. A. and Scholz, C. H. (1992b). Displacement–length scaling relationship for faults data synthesis and discussion. *J. Struct. Geol.*, **14**, 1149–1156.
Cowie, P. A., Scholz, C. H., Edwards, M., and Malinverno, A. (1993). Fault strain and seismic coupling on mid-ocean ridges. *J. Geophys. Res.*, **98**, 17 911–17 920.
Crosby, A. and McKenzie, D. (2005). Measurements of elastic thickness under ancient lunar terrain. *Icarus*, **173**, 100–107.
Dawers, N. H. and Anders, M. H. (1995). Displacement–length scaling and fault linkage, *J. Struct. Geol.*, **17**, 607–614.
Dawers, N. H., Anders, M. H., and Scholz, C. H. (1993). Growth of normal faults: displacement–length scaling. *Geology*, **21**, 1107–1110.
Dombard, A. J. and Gillis, J. J. (2001). Testing the viability of topographic relaxation as a mechanism for the formation of lunar floor-fractured craters. *J. Geophys. Res.*, **106**, 27 901–27 910.
Ewing, M., Latham, G., Press, F., Sutton, G., Dorman, J., Nakamura, Y., Meissner, R., Duennebier, F., and Kovach, R. (1971). Seismology of the Moon and implications on internal structure, origin and evolution (abs.). In *Highlights of Astronomy*, ed. C. De Jager. Dordrecht: Reidel, pp. 155–172.
Fielder, G. (1961). *Structure of the Moon's Surface*. New York, NY: Pergamon.
Freed, A. M., Melosh, H. J., and Solomon, S. C. (2001). Tectonics of mascon loading: Resolution of the strike-slip faulting paradox. *J. Geophys. Res.*, **106**, 20 603–20 620.
Gagnepain-Beyneix, J., Lognonné, P., Chenet, H., and Spohn, T. (2006). Seismic models of the Moon and constraints on temperature and mineralogy. *Phys. Earth Planet. Inter.*, **159**, 140–166.
Gilbert, G. K. (1893). The Moon's face, a study of the origin of its features. *Philos. Soc. Washington Bull.*, **12**, 241–292.
Gillespie, P. A., Walsh, J. J., and Watterson, J. (1992). Limitations of dimension and displacement data from single faults and the consequences for data analysis and interpretation. *J. Struct. Geol.*, **14**, 1157–1172.
Goins, N. R., Dainty, A. M., and Toksöz, M. N. (1981). Seismic energy release of the Moon. *J. Geophys. Res.*, **86**, 378–388.
Golombek, M. P. (1979). Structural analysis of lunar grabens and the shallow crustal structure of the Moon. *J. Geophys. Res.*, **84**, 4657–4666.
Golombek, M. P. (1985). Fault type predictions from stress distributions on planetary surfaces: Importance of fault initiation depth. *J. Geophys. Res.*, **90**, 3065–3074.
Golombek, M. P. and McGill, G. E. (1983). Grabens, basin tectonics, and the maximum total expansion of the Moon. *J. Geophys. Res.*, **88**, 3563–3578.
Golombek, M. P., Plescia, J. B., and Franklin, B. J. (1991). Faulting and folding in the formation of planetary wrinkle ridges. *Proc. Lunar Planet Sci. Conf. 21*, 679–693.
Golombek, M. P., Anderson, F. S., and Zuber, M. T. (2001). Martian wrinkle ridge topography: Evidence for subsurface faults from MOLA. *J. Geophys. Res.*, **106**, 23 811–23 821.
Greeley, R. (1971). Lunar Hadley Rille: Considerations of its origin. *Science*, **172**, 722–725.
Greeley, R. and Spudis, P. D. (1978). Mare volcanism in the Herigonius region of the Moon. *Proc. Lunar Planet. Sci. Conf. 9*, 3333–3349.
Hall, J. L., Solomon, S. C., and Head, J. W. (1981). Lunar floor-fractured craters: Evidence for viscous relaxation of crater topography. *J. Geophys. Res.*, **86**, 9537–9552.
Hardacre, K. M. and Cowie, P. A. (2003). Controls on strain localization in a two-dimensional elastoplastic layer: Insights into size-frequency scaling of extensional fault populations. *J. Geophys. Res.*, **108**, 2529.

Hartmann, W. K. and Wood, C. A. (1971). Moon: Origin and evolution of multiring basins. *The Moon*, **3**, 3–78.

Head, J. W. (1976). Lunar volcanism in space and time. *Rev. Geophys. Space Phys.*, **14**, 265–300.

Hiesinger, H. and Head, J. W. (2006). New views of lunar geoscience: An introduction and overview. *Rev. Mineral. Geochem.*, **60**, 1–81.

Hiesinger, H., Jaumann, R., Neukam, G., and Head, J. W. (2000). Ages of mare basalts on the lunar nearside. *J. Geophys. Res.*, **105**, 29 239–29 276.

Hiesinger H., Head III, J. W., Wolf, U., Jaumann, R., and Neukum, G. (2003). Ages and stratigraphy of mare basalts in Oceanus Procellarum, Mare Nubium, Mare Cognitum, and Mare Insularum. *J. Geophys. Res.*, **108** (E7), 5065, doi:10.1029/2002JE001985.

Hodges, C. A. (1973). Mare ridges and lava lakes. *Apollo 17 Prel. Sci. Rep., NASA Spec. Publ.*, **SP-330**, 31–12 – 31–21.

Hood, L. L., Mitchell, D. L., Lin, R. P., Acuna, M. H., and Binder, A.B. (1999). Initial measurements of the lunar induced magnetic dipole moment using Lunar Prospector magnetometer data. *Geophys. Res. Lett.*, **26**, 2327–2330.

Howard, K. A. and Muehlberger, W. R. (1973). Lunar thrust faults in the Taurus–Littrow region. *Apollo 17 Prel. Sci. Rep., NASA Spec. Publ.*, **SP-330**, 31–32 – 31–25.

Johnson, A. M. (1980). Folding and faulting of strain-hardening sedimentary rocks. *Tectonophysics*, **62**, 251–278.

Khan, A. and Mosegaard, K. (2002). An inquiry into the lunar interior – A non linear inversion of the Apollo seismic data. *J. Geophy. Res.*, **107**, doi:10.1029/2001JE001658.

Khan, A., Maclennan, J., Taylor, S. R., and Connolly, J. A. D. (2006). Are the Earth and the Moon compositionally alike? Inferences on lunar composition and implications for lunar origin and evolution from geophysical modeling. *J. Geophys. Res.*, **111**, E05005, doi:10.1029/2005JE002608.

Khan, A., Connolly, J. A. D., Olsen, N., and Mosegaard, K. (2007). Constraining the composition and thermal state of the moon from an inversion of electromagnetic lunar day-side transfer functions (abs.). *Lunar Planet. Sci. Conf. XXXVIII*, 1086. Houston, TX: Lunar and Planetary Institute (CD-ROM).

Konopliv, A. S. and Yuan, D. N. (1999). Lunar Prospector 100th degree gravity model development. *Proc. Lunar Planet. Sci. Conf. 30*, 1067–1068.

Konopliv, A. S., Binder, A. B., Hood, L. L., Kucinskas, A. B., Sjogren, W. L., and Williams, J. G. (1998). Improved gravity field of the Moon from Lunar Prospector. *Science*, **281**, 1476–1480.

Konopliv, A. S., Asmar, S. W., Carranza, E., Sjogren, W. L., and Yuan, D. N. (2001). Recent gravity models as a result of the Lunar Prospector mission. *Icarus*, **150**, 1–18.

Lammlein, D. R. (1973). *Lunar seismicity, structure and tectonics*. PhD dissertation, Columbia University, New York.

Lammlein, D. (1977). Lunar seismicity and tectonics. *Phys. Earth Planet. Inter.*, **14**, 224–273.

Lammlein, D., Latham, G. V., Dorman, J., Nakamura, Y., and Ewing, M. (1974). Lunar seismicity, structure and tectonics. *Rev. Geophys. Space Phys.*, **12**, 1–21.

Lemoine, F. G. R., Smith, D. E., Zuber, M. T., Neumann, G. A., and Rowlands, D. D. (1997). A 70th degree lunar gravity model (GLGM-2) from Clementine and other tracking data. *J. Geophys. Res.*, **102**, 16 339–16 359.

Lognonné, P. and Johnson, C. L. (2007). Planetary seismology. In *Treatise on Geophysics*, Vol. 10, Ch. 4., ed. G. Schubert. New York: Elsevier.

Lognonné, P., Gagnepain-Beyneix, J., and Chenet, H. (2003). A new seismic model of the Moon: Implication in terms of structure, formation and evolution. *Earth Plan. Sci. Lett.*, **6637**, 1–18.

Lucchitta, B. K. (1976). Mare ridges and related highland scarps: Results of vertical tectonism. *Geochim. Cosmochim. Acta*, **3**, (Suppl.), 2761–2782.

Lucchitta, B. K. (1977). Topography, structure, and mare ridges in southern Mare Imbrium and northern Oceanus Procellarum. *Proc. Lunar Sci. Conf. 8*, *Geochim. Cosmochim. Acta*, **3**, (Suppl.), 2691–2703.

Lucchitta, B. K. and Watkins, J. A. (1978). Age of graben systems on the Moon. *Proc. Lunar Planet. Sci. Conf. 9*, *Geochim. Cosmochim. Acta*, **3**, (Suppl.), 3459–3472.

Margot, J. L., Campbell, D. B., Jurgens, R. F., Slade, M. A., and Stacy, N. J. (1998). The topography of the lunar polar regions from Earth-based radar interferometry (abs.). *Lunar Planet. Sci. Conf. 29*, 1845. Houston, TX: Lunar and Planetary Institute (CD-ROM).

Margot, J. L., Campbell, D. B., Jurgens, R. F., and Slade, M. A. (1999). Topography of the lunar poles from radar interferometry: a survey of cold trap locations. *Science*, **284**, 1658, doi:10.1126/science.284.5420.1658.

Marrett, R. and Allmendinger, R. W. (1991). Estimates of strain due to brittle faulting: sampling of fault populations. *J. Struct. Geol.*, **13**, 735–738.

Masursky, H., Colton, G. W., and El-Baz, F. (1978). Apollo over the Moon: A view from orbit. *NASA Spec. Publ.*, **SP-362**.

Mattingly, T. K., El-Baz, F., and Laidley, R. A. (1972). Observations and impressions from lunar orbit. *Apollo 16 Prel. Sci. Rep.*, 28–1 – 28–16.

Maxwell, T. A. (1978). Origin of multi-ring basin ridge systems: An upper limit to elastic deformation based on a finite-element model. (Proc. Lunar Planet. Sci. Conf. 9), *Geochim. Cosmochim. Acta*, **3**, (Suppl.), 3541–3559.

Maxwell, T.A. and Phillips, R. J. (1978). Stratigraphic correlation of the radar-detected subsurface interface in Mare Crisium. *Geophys. Res. Lett.*, **5**, 811–814.

Maxwell, T. A., El-Baz, F., and Ward, S. W. (1975). Distribution, morphology, and origin of ridges and arches in Mare Serenitatis. *Geol. Soc. Am. Bull.*, **86**, 1273–1278.

McCauley, J. F. (1969). Geologic map of the Alphonsus region Ga region of the Moon. U.S. Geol. Surv. Map 1–586, scale 1:50 000.

McGill, G. E. (1971). Attitude of fractures bounding straight and arcuate lunar rilles. *Icarus*, **14**, 53–58.

McGill, G. E. (2000). Fault growth by segment linkage: an explanation for scatter in maximum displacement and trace length data from the Canyonlands grabens of SE Utah: Discussion. *J. Struct. Geol.*, **22**, 135–140.

Mege, D. and Reidel, S. P. (2001). A method for estimating 2D wrinkle ridge strain from application of fault displacement scaling to the Yakima folds, Washington. *Geophys. Res. Lett.*, **28**, 3545–3548.

Melosh, H. J. (1978). The tectonics of mascon loading. *Proc. Lunar Planet. Sci. Conf. 9*, 3513–3525.

Melosh, H. J. and McKinnon, W. B. (1988). The tectonics of Mercury. In *Mercury*, ed. F. Vilas, C. R. Chapman and M. S. Matthews. Tucson, AZ: University of Arizona Press, pp. 374–400.

Melosh, H. J. and Williams, C. A., Jr. (1989). Mechanics of graben formation in crustal rocks: A finite element analysis. *J. Geophys. Res.*, **94**, 13 961–13 973.

Minshull, T. A. and Goulty, N. R. (1988). The influence of tidal stresses on deep moonquake activity. *Phys. Earth Planet. Inter.*, **52**, 41–55.

Moore, J. M. and Schultz, R. A. (1999). Processes of faulting in jointed rocks of Canyonlands National Park. *Geol. Soc. Am. Bull.*, **111**, 808–822.

Muehlberger, W. R. (1974). Structural history of southeastern Mare Serenitatis and adjacent highlands. *Proc. Lunar Sci. Conf. 5, Geochim. Cosmochim. Acta*, **1**, (Suppl.), 101–110.

Mueller, K. and Golombek, M. P. (2004). Compressional structures on Mars. *Annu. Rev. Earth Planet. Sci.*, doi:10.1146/annurev.earth.1132.101802.120553.

Muller, P. M. and Sjogren, W. L. (1968). Masons: lunar mass concentrations. *Science*, **161**, 680–684.

Nakamura, Y. (1977). HFT events: shallow moonquakes? *Phys. Earth Planet. Inter.*, **14**, 217–223.

Nakamura, Y. (1980). Shallow moonquakes: How they compare with earthquakes. *Proc. Lunar Planet. Sci. Conf. 11*, 1847–1853.

Nakamura, Y. (1983). Seismic velocity structure of the lunar mantle. *J. Geophys. Res.*, **88**, 677–686.

Nakamura, Y. (2003). New identification of deep moonquakes in the Apollo lunar seismic data. *Phys. Earth Planet. Inter.*, **139**, 197–205.

Nakamura, Y. (2005). Farside deep moonquakes and deep interior of the Moon. *J. Geophys. Res.*, **110**, E01001, doi:10.1029/2004JE002332.

Nakamura, Y. (2007). Within-nest hypocenter distribution and waveform polarization of deep moonquakes and their possible implications (abs.). *Lunar Planet. Sci. Conf. XXXVIII*, 1160. Houston, TX: Lunar and Planetary Institute (CD-ROM).

Nakamura, Y., Duennebier, F. K., Latham, G. V., and Dorman, H. J. (1976). Structure of the lunar mantle. *J. Geophys. Res.*, **81**, 4818–4824.

Nakamura, Y., Latham, G. V., Dorman, H. J., Ibrahim, A.-B. K., Koyama, J., and Horvath, P. (1979). Shallow moonquakes: Depth, distribution and implications as to the present state of the lunar interior. *Proc. Lunar Sci. Conf. 10*, 2299–2309.

Nakamura, Y., Latham, G. V., Dorman, J., and Harris, J. (1981). Passive seismic experiment long-period event catalog: Final version. *Technical Report* No. 18, Galveston Geophysics Laboratory, University of Texas at Austin.

Neukum, G. and Ivanov, B. A. (1994). Crater size distributions and impact probabilities on Earth from lunar, terrestrial-planet, and asteroid cratering data, hazards due to comets and asteroids. In *Space Science Series*, ed. T. Gehrels, M. S. Matthews and A. Schumann. Tucson, AZ: University of Arizona Press, 359.

Neumann, G. A., Zuber, M. T., Smith, D. E., and Lemoine, F. G. (1996). The lunar crust: Global structure and signature of major basins. *J. Geophys. Res.*, **101**, 16 843–16 863.

Nino, P., Philip, H., and Chery, J. (1998). The role of bed-parallel slip in the formation of blind thrust faults. *J. Struct. Geol.*, **20**, 503–516.

Nozette, S., Rustan, P., Pleasance, L. P., Kordas, J. F., Lewis, I. T., Park, H. S., Priest, R. E., Horan, D. M., Regeon, P., Lichtenberg, C. L., Shoemaker, E. M., Eliason, E. M., McEwen, A. S., Robinson, M. S., Spudis, P. D., Acton, C. H., Buratti, B. J., Duxbury, T. C., Baker, D. N., Jakosky, B. M., Blamont, J. E., Corson, M. P., Resnick, J. H., Rollins, C. J., Davies, M. E., Lucey, P. G., Malaret, E., Massie, M. A., Pieters, C. M., Reisse, R. A., Simpson, R. A., Smith, D. E., Sorenson, T. C., Vorder Breugge, R. W., and Zuber, M. T. (1994). The Clementine mission to the Moon: Scientific overview. *Science*, **266**, 1835–1839.

Oberst, J. (1987). Unusually high stress drops associated with shallow moonquakes. *J. Geophys. Res.*, **92**, 1397–1405.

Ockendon, J. R. and Turcotte, D. L. (1977). On the gravitational potential and field anomalies due to thin mass layers. *Geophys. J.*, **48**, 479–492.

Ono, T., Kumamoto, A., Nakagawa, H., Yamaguchi, Y., Oshigami, S., Yamaji, A., Kobayashi, T., Kasahara, Y., and Oya, H. (2009). Lunar radar sounder observations of subsurface layers under the nearside maria of the Moon. *Science*, **323**, 909–912.

Peeples, W. J., Sill, W. R., May, T. W., Ward, S. H., Philips, R. J., Jordan, R. L., Abbott, E. A., and Killpack, T. J. (1978). Orbital radar evidence for Lunar subsurface layering in Maria Serenitatis and Crisium. *J. Geophys. Res.*, **83**, 3459–3468.

Phillips, R. J., Conel, J. E., Abbott, E. A., Sjogren, W. L., and Morton, J. B. (1972). Mascons: Progress toward a unique solution for mass distribution. *J. Geophys. Res.*, **77**, 7106–7114.

Phillips, R. J., Adams, G. F., Brown, W. E., Jr., Eggleton, R. E., Jackson, P., Jordan, R., Peeples, W. J., Porcello, L. J., Ryu, J., Schaber, G., Sill, W. R., Thompson, T. W., Ward, S. H., and Zelenka, J. S. (1973). The Apollo 17 Lunar Sounder (Proc. Lunar Science Conf. 4). *Geochim. Cosmochim. Acta*, **3**, (Suppl. 4), 2821–2831.

Pike, R. J. (1971). Genetic implications of the shapes of Martian and lunar craters. *Icarus*, **15**, 384–395.

Plescia, J. B. and Golombek, M. P. (1986). Origin of planetary wrinkle ridges based on the study of terrestrial analogs. *Geol. Soc. Am. Bull.*, **97**, 1289–1299.

Pritchard, M. E. and Stevenson, D. J. (2000). Thermal aspects of a lunar origin by giant impact. In *Origin of the Earth and Moon*, ed. R. Canup, and K. Righter. Tucson, AZ: University of Arizona Press, pp. 179–196.

Quaide, W. L. (1965). Rilles, ridges, and domes: Clues to maria history. *Icarus*, **4**, 374.

Raitala, J. (1984). Terra scarps indicating youngest terra faults on the Moon. *Earth, Moon, and Planets*, **31**, 63–74.

Reidel, S. P. (1984). The Saddle Mountains: The evolution of an anticline in the Yakima fold belt. *Am. Jour. Sci.*, **284**, 942–978.

Robinson, M. S. and Joliff, B. L. (2002). Apollo 17 landing site: Topography, photometric corrections, and heterogeneity of the surrounding highland massifs. *J. Geophys. Res. Planets*, **107**, 20–1, E11, 5110, doi:10.1029/2001JE001614.

Roering, J. J., Cooke, M. L., and Pollard, D. D. (1997). Why blind thrust faults do not propagate to the Earth's surface: Numerical modeling of coseismic deformation associated with thrust-related anticlines. *J. Geophys. Res.*, **102**, 12 901–12 912.

Rosiek, M. R., Cook, A. C., Robinson, M. S., Watters, T. R., Archinal, B. A., Kirk, R. L., and Barrett, J. M. (2007). A revised planet-wide digital elevation model of the moon (abs.), *Lunar Planet. Sci. Conf. XXXVIII*, 2297. Houston, TX: Lunar and Planetary Institute (CD-ROM).

Schaber, G. G. (1973a). Lava flows in Mare Imbrium: Geologic evaluation from Apollo orbital photography. *Proc. Lunar Sci. Conf. 4*, 73–92.

Schaber, G. G. (1973b). Eratosthenian volcanism in Mare Imbrium: Sources of youngest lava flows. *Apollo 17 Prel. Sci. Rep., NASA Spec. Publ.*, **SP-330**, 31–22 – 31–25.

Schaber, G. G., Boyce, J. M., and Moore, H. J. (1976). The scarcity of mappable flow lobes on the lunar maria: Unique morphology of the Imbrium flows. *Proc. Lunar Sci. Conf. 7*, 2783–2800.

Schenk, P. M., and Bussey, B. J. (2004). Galileo stereo topography of the lunar north polar region. *Geophys. Res. Lett.*, **31**, L23701.

Schmitt, H. H. and Cernan, E. A. (1973). Geological investigation of the Apollo 17 landing site. *Apollo 17 Prel. Sci. Rep., NASA Spec. Publ.*, **SP-330**, 5–1 – 5–21.

Scholz, C. H. and Cowie, P. A. (1990). Determination of geologic strain from fault slip data. *Nature*, **346**, 837–839.

Schultz, P. H. (1976a). *Moon Morphology: Interpretations Based on Lunar Orbiter Photography*. Austin, TX: University of Texas Press.

Schultz, P. H. (1976b). Floor-fractured lunar craters. *The Moon*, **15**, 241–273.
Schultz, P. H., Staid, M. I., and Pieters, C. M. (2006). Lunar activity from recent gas release. *Nature*, **444**, 184–186, doi:10.1038/nature05303.
Schultz, R. A. (1997). Displacement–length scaling for terrestrial and Martian faults: Implications for Valles Marineris and shallow planetary grabens. *J. Geophys. Res.*, **102**, 12 009–12 015.
Schultz, R. A. (1999). Understanding the process of faulting: Selected challenges and opportunities at the edge of the 21st century. *J. Struct. Geol.*, **21**, 985–993.
Schultz, R. A. (2000). Localizaton of bedding-plane slip and backthrust faults above blind thrust faults: Keys to wrinkle ridge structure. *J. Geophys. Res.*, **105**, 12 035–12 052.
Schultz, R. A. and Fori, A. N. (1996). Fault-length statistics and implications of graben sets at Candor Mensa, Mars. *J. Struct. Geol.*, **18**, 272–383.
Schultz, R. A. and Zuber, M. A. (1994). Observations, models, and mechanisms of failure of surface rocks surrounding planetary surface loads. *J. Geophys. Res.*, **99**, 14 691–14 702.
Scott, D. H. (1973). Small structures of the Taurus-Littrow region. *Apollo 17 Prel. Sci. Rep., NASA Spec. Publ.*, **SP-330**, pp. 31–25 – 31–29.
Scott, D. H., Diaz, J. M., and Watkins, J. A. (1977). Lunar farside tectonics and volcanism. *Proc. Lunar Sci. Conf. 8*, 1119–1130.
Sharpton, V. L. (1992). Apollo 17: One giant step toward understanding the tectonic evolution of the Moon: Geology of the Apollo 17 landing site. *LPI Tech. Rep. 92–09, Part 1*, 50–53.
Sharpton, V. L. and Head, J. W. (1981). The origin of mare ridges: Evidence from basalt stratigraphy and substructure in Mare Serenitatis (abs.). *Lunar Planet. Sci. Conf. XII*, 961–963.
Sharpton, V. L. and Head, J. W. (1982). Stratigraphy and structural evolution of southern Mare Serenitatis: A reinterpretation based on Apollo Lunar Sounder Experiment data. *J. Geophys. Res.*, **87**, 10 983–10 998.
Sharpton, V. L. and Head, J. W. (1988). Lunar mare ridges: Analysis of ridge-crater intersection and implications for the tectonic origin of mare ridges. *Proc. Lunar Sci. Conf. 18*, 307–317.
Shearer, C. K., Hess, P. C., Wieczorek, M. A., Pritchard, M. E., Permentier, E. M., Borg, L. E., Longhi, J., Elkins-Tanton, L. T., Neal, C. R., Antonenko, I., Canup, R. M., Halliday, A. N., Grove, T. L., Hager, B. H., Less, D.-C., and Wiechert, U. (2006). Thermal and magmatic evolution of the Moon. *Rev. Mineral. Geochem.*, **60**, 365–518.
Simpson, R. W. (1997). Quantifying Anderson's fault types. *J. Geophys. Res.*, **102**, 17 909–17 920.
Smith, D. E., Zuber, M. T., Neumann, G. A., and Lemoine, F. G. (1997). Topography of the Moon from the Clementine LIDAR. *J. Geophys. Res.*, **102**, 1591–1611.
Solomon, S. C. and Chaiken, J. (1976). Thermal expansion and thermal stress in the Moon and terrestrial planets: Clues to early thermal history. *Proc. Lunar Sci. Conf. 7*, 3229–3243.
Solomon, S. C. and Head, J. W. (1979). Vertical movement in mare basins: Relation to mare emplacement, basin tectonics and lunar thermal history. *J. Geophys. Res.*, **84**, 1667–1682.
Solomon, S. C. and Head, J. W. (1980). Lunar mascon basins: Lava filling, tectonics, and evolution of the lithosphere. *Rev. Geophys. Space Phys.*, **18**, 107–141.
Spudis, P. D. (1993). *The Geology of Multi-Ring Impact Basins: The Moon and Other Planets*. Cambridge: Cambridge University Press.

Spudis, P. D., Swann, G. A., and Greeley, R. (1988a). The formation of Hadley Rille and implications for the geology of the Apollo 15 region. *Proc. Lunar Sci. Conf. 18*, 243–254.

Spudis, P. D., Hawke, B. R., and Lucey, P. G. (1988b). Materials and formation of the Imbrium Basin. *Proc. Lunar Sci. Conf. 18*, 155–168.

Spudis, P. D., Reisse, R. A., and Gillis, J. J. (1994). Ancient multiring basins on the Moon revealed by Clementine laser altimetry. *Science*, **266**, 1848–1851.

Stöffler, D. and Ryder, G. (2001). Stratigraphy and isotope ages of lunar geologic units: Chronological standard for the inner Solar System. *Space Sci. Rev.*, **96**, 9–54.

Strom, R. G. (1972). Lunar mare ridges, rings, and volcanic ring complexes. *Mod. Geol.*, **2**, 133–157.

Tjia, H. D. (1970). Lunar wrinkle ridges indicative of strike-slip faulting. *Geol. Soc. Am. Bull.*, **81**, 3095–3100.

Toksöz, M. N. (1974). Geophysical data and the interior of the Moon. *Annu. Rev. Earth Planet. Sci.*, **2**, 151.

Toksöz, M. N., Goins, N. R., and Cheng, C. H. (1977). Moonquakes: Mechanisms and relations to tidal stresses. *Science*, **196**, 979–981.

U. S. Geological Survey (USGS) (1972). Preliminary topographic map of part of the Littrow region of the Moon, scale 1:50 000. Flagstaff, AZ.

U. S. Geological Survey (USGS) (2002). Color-coded topography and shaded relief of the lunar north and south hemispheres, U.S. Geol. Surv. Geol. Invest. Ser., 2769.

Vinnik, L., Chenet, H., Gagnepain-Beyneix, J., and Lognonné, P. (2001). First seismic receiver functions on the Moon. *Geophys. Res. Lett.*, **28**, 3031–3034.

Walsh, J. and Watterson, J. (1988). Analysis of the relationship between displacements and dimensions of faults. *J. Struct. Geol.*, **10**, 239–247.

Watters, T. R. (1988). Wrinkle ridge assemblages on the terrestrial planets. *J. Geophys. Res.*, **93**, 10 236–10 254.

Watters, T. R. (1991). Origin of periodically spaced wrinkle ridges on the Tharsis plateau of Mars. *J. Geophys. Res.*, **96**, 15 599–15 616.

Watters, T. R. (1992). A system of tectonic features common to Earth, Mars, and Venus. *Geology*, **20**, 609–612.

Watters, T. R. (1993). Compressional tectonism on Mars. *J. Geophys. Res.*, **98**, 17 049–17 060.

Watters, T. R. (2003). Thrust faulting along the dichotomy boundary in the eastern hemisphere of Mars. *J. Geophys. Res.*, **108**, 5055, doi:10.1029/2002JE001934.

Watters, T. R. (2004). Elastic dislocation modeling of wrinkle ridges on Mars. *Icarus*, **171**, 284–294.

Watters, T. R. and Konopliv, A. S. (2001). The topography and gravity of Mare Serenitatis: Implications for subsidence of the mare surface. *Planet. Space Sci.*, **49**, 743–748.

Watters, T. R. and Robinson, M. S. (1997). Radar and photoclinometric studies of wrinkle ridges on Mars. *J. Geophys. Res.*, **102**, 10 889–10 904.

Watters, T. R. and Robinson, M. S. (1999). Lobate scarps and the Martian crustal dichotomy. *J. Geophys. Res.*, **104**, 18 981–18 900.

Watters, T. R., Robinson, M. S., and Cook, A. C. (1998). Topography of lobate scarps on Mercury: New constraints on the planet's contraction. *Geology*, **26**, 991–994.

Watters, T. R., Robinson, M. S., and Schultz, R. A. (2000). Displacement–length relations of thrust faults associated with lobate scarps on Mercury and Mars: Comparison with terrestrial faults. *Geophys. Res. Lett.*, **27**, 3659–3662.

Watters, T. R., Robinson, M. S., and Cook, A. C. (2001). Large-scale lobate scarps in the southern hemisphere of Mercury. *Planet. Space Sci.*, **49**, 1523–1530.

Watters, T. R., Robinson, M. S., Bina, C. R., and Spudis, P. D. (2004). Thrust faults and the global contraction of Mercury. *Geophys. Res. Lett.*, **31**, L04701, doi:10.1029/2003GL019171.

Watters, T. R., Nimmo, F., and Robinson, M. S. (2005). Extensional troughs in the Caloris Basin of Mercury: Evidence of lateral crustal flow. *Geology*, **33**, 669–672.

Watters, T. R., Solomon, S. C., Robinson, M. S., Head, J. W., André, S. L., Hauck, S. A., and Murchie, S. L. (2009). The tectonics of Mercury: The view after MESSENGER'S first flyby. *Earth Planet. Sci. Lett.*, doi:10.1016/j.epsl.2009.01.025.

Weber (formerly Bulow), R., Bills, B. G., and Johnson, C. L. (2009). Constraints on deep moonquake focal mechanisms through analyses of tidal stress. *J. Geophys. Res. Planets*, **114**, E05001, doi:10.1029/2008JE003286.

Whitaker, E. A. (1966). The surface of the Moon. In *The Nature of the Lunar Surface: Proceedings of the 1965 IAU-NASA Symposium*, ed. W. N. Hess, D. H. Menzel and J. A. O'Keefe. Baltimore, MD: Johns Hopkins Press, pp. 79–98.

Wichman, R. W. and Schultz, P. H. (1995). Floor-fractured craters in Mare Smythii and west of Oceanus Procellarum: Implications of crater modification by viscous relaxation and igneous intrusion models. *J. Geophys. Res.*, **100**, 21 201–21 218.

Wieczorek, M. A. and Phillips, R. J. (1998). Potential anomalies on a sphere: Applications to the thickness of the lunar crust. *J. Geophys. Res.*, **103**, 1715–1724.

Wieczorek, M. A. and Simons, F. J. (2005). Localized spectral analysis on the sphere. *Geophys. J. Int.*, **162**, 655–675.

Wieczorek, M. A., Jolliff, B. L., Khan, A., Pritchard, M. E., Weiss, B. P., Williams, J. G., Hood, L. L., Righter, K., Neal, C. R., Shearer, C. K., McCallum, I. S., Tompkins, S., Hawke, B. R., Peterson, C., Gillis, J. J., and Bussey, B. (2006). The constitution and structure of the lunar interior. *Rev. Mineral. Geochem.*, **60**, 221–364.

Wilhelms, D. E. (1987). *The Geologic History of the Moon*. Washington, DC: U.S. Government Printing Office.

Wilhelms, D. E. and McCauley, J. F. (1971). Geologic map of the near side of the Moon. USGS Map I-703, scale 1:5 000 000.

Williams, J. G., Boggs, D. H., Yoder, C. F., Ratcliff, J. T., Todd, J., and Dickey, J. O. (2001). Lunar rotational dissipation in solid body and molten core. *J. Geophys. Res.*, **106**, 27 933–27 968.

Wise, D. U. and Yates, M. T. (1970). Mascons as structural relief on a lunar "Moho". *J. Geophys. Res.*, **75**, 261–268.

Weisberg, O. and Hager, B. H. (1998). Global lunar contraction with subdued surface topography (abs.): *Origin of the Earth and Moon*, LPI contribution no. 957. Houston, TX: Lunar and Planetary Institute, p. 54.

Wojtal, S. F. (1996). Changes in fault displacement populations correlated to linkage between faults. *J. Struct. Geol.*, **18**, 265–279.

Wollenhaupt, W. R., Sjogren, W. L., Lingenfelter, R. E., Schubert, G., and Kaula, W. M. (1973). Apollo 17 Laser Altimeter. *Apollo 17 Prel. Sci. Rep., NASA Spec. Publ.*, **SP-330**, 33–41 – 33–44.

Wu, S. S. C. and Doyle, F. J. (1990). Topographic mapping. In *Planetary Mapping*, ed. R. Greeley and R. M. Batson. Cambridge: Cambridge University Press, pp. 169–207.

Young, R. A., Brennan, W. J., Wolfe, R. W., and Nichols, P. J. (1973). Volcanism in the lunar maria. *Apollo 17 Prel. Sci. Rep., NASA Spec. Publ.*, **SP-330**, 31–1 – 31–11.

Zuber, M. T., Smith, D. E., Lemoine, F. G., and Neumann, G. A. (1994). The shape and internal structure of the Moon from the Clementine Mission. *Science*, **266**, 1839–1843.